19. Radiation and Optics in the Atmosphere

This chapter describes the fundamentals of radiation transport in general and in the Earth's atmosphere. The role of atmospheric aerosol and clouds are discussed and the connections between radiation and climate are described. Finally, natural optical phenomena of the atmosphere are discussed.

There are a multitude of processes in which electromagnetic radiation interacts with the atmosphere:

- Absorption, i. e. radiation is removed from the radiation field and converted into some other form of energy, e.g. heat. Absorption can be due to molecules in the atmosphere (such as ozone, oxygen, or water vapor) or aerosols (such as soot), absorption of solar energy in the atmosphere is an important process in the climate system of the Earth.
- Elastic scattering, which – seen from an individual photon – changes its direction of propagation, but not its energy (and hence wavelength or 'color'). Scattering can be due to molecules (Rayleigh scattering) or aerosol particles (Mie scattering) present in the air.
- Inelastic scattering where, as for elastic scattering, the direction of a photon is changed but where its energy is also changed. Inelastic scattering by molecules is called Raman scattering, where the energy of the scattered photon can be reduced at the expense of energy transferred to the scattering molecule (Stokes scattering). Likewise, energy can be transferred from the (thermally excited) molecules to the photon (anti-Stokes scattering).
- Thermal emission from air molecules and aerosol particles. The emission at any given wavelength cannot exceed the Planck function (or emission from a black body) for the temperature of the atmosphere, thus noticeable thermal emission only takes place at infrared wavelengths longer than several micrometers. Due to Kirchhoff's law only absorbing gases (such as CO_2, H_2O, O_3, but not the main components of air N_2, O_2, Ar), can emit radiation.

- Aerosol fluorescence. Excitation of molecules within aerosol particles by radiation can result in (broad band) fluorescence; this process will not be further discussed here.

19.1 Radiation Transport in the Earth's Atmosphere

In the following we introduce the basic quantities pertinent to the propagation of radiation in the atmosphere and discuss the fundamental laws governing radiation transport in absorbing and scattering media, i.e. the atmosphere.

19.1.1 Basic Quantities Related to Radiation Transport

A light source will emit a certain amount W of energy in the form of radiation.

1. The radiant flux Φ is defined as the radiation energy W per unit time (regardless of the direction in which it is emitted):

$$\Phi = \frac{\text{radiated energy}}{\text{time interval}} = \frac{\mathrm{d}W}{\mathrm{d}t} \quad \left[\frac{\mathrm{W\,s}}{\mathrm{s}} = \mathrm{W} \right]$$
(19.1)

2. The irradiance B is defined as the radiant flux Φ received by an ('illuminated') area A_e:

$$B = \frac{\Phi}{A_e} \quad \left[\frac{W}{m^2} \right] ;$$
(19.2)

3. The radiation intensity is ($\Omega = $ solid angle):

$$I = \frac{\Phi}{\Omega} \quad [\mathrm{W/sr}] ;$$
(19.3)

4. The radiance is ($A_s = $ radiating area):

$$F = \frac{\Phi}{\Omega A_s} \quad \left[\frac{W}{m^2 sr} \right] .$$
(19.4)

(All areas are assumed to be oriented perpendicular to the direction of propagation of the radiation.)

19.1.2 Absorption Processes

Radiation is absorbed by molecules in the atmosphere (such as ozone, oxygen, or water vapor), aerosol (such as soot) or liquid and solid water particles (cloud droplets (ice crystals)). Absorption of solar ultraviolet (UV) radiation at wavelengths below about 300 nm by atmospheric O_2 and O_3 is important for life on Earth.

19.1.3 Rayleigh Scattering

Elastic scattering (i.e. scattering without change of the photon energy) by air molecules is called Rayleigh scattering. While this is not an absorption process, light scattered out of the probing light beam will normally not reach the detector, thus for narrow beams it is justified to treat Rayleigh scattering as an absorption process. The Rayleigh scattering cross section $\sigma_R(\lambda)$ (in cm^2) is given by [19.1]:

$$\sigma_R(\lambda) = \frac{24\pi^3}{\lambda^4 N_{air}^2} \frac{\left[n_0(\lambda)^2 - 1 \right]^2}{\left[n_0(\lambda)^2 + 2 \right]^2} F_K(\lambda)$$

$$\approx \frac{8\pi^3}{3\lambda^4 N_{air}^2} \left[n_0(\lambda)^2 - 1 \right]^2 F_K(\lambda) ,$$
(19.5)

where: λ denotes the wavelength, $n_0(\lambda)$ is the real part of the wavelength-dependent index of refraction of air, N_{air} is the number density of air (e.g. 2.4×10^{19} molec/cm^3 at $20\,°C$, 1 atm), $F_K(\lambda) \approx 1.061$ is a correction for anisotropy (polarisability of air molecules).

Note that $n_0(\lambda)^2 - 1 \approx 2[n_0(\lambda) - 1] \propto N_{air}$, since $n_0 \approx 1$ [in fact n_0 (550 nm) = 1.000293], and $n_0 - 1 \propto N_{air}$, thus $\sigma_R(\lambda)$ is essentially independent of N_{air}. On that basis a simplified expression for the Rayleigh scattering cross section (in cm^2) is given by *Nicolet* [19.2]

$$\sigma_R(\lambda) \approx \frac{4.02 \times 10^{-28}}{\lambda^{4+x}}$$
(19.6)

with

$$x = 0.04$$
$$\quad \text{for} \quad \lambda > 0.55\,\mu m ,$$
$$x = 0.389\lambda + 0.09426/\lambda - 0.3328$$
$$\quad \text{for} \quad 0.2\,\mu m < \lambda < 0.55\,\mu m .$$

For these simple estimates the Rayleigh scattering cross section can be written as

$$\sigma_R(\lambda) \approx \sigma_{R_0} \lambda^{-4}$$
$$\left(\sigma_{R_0} \approx 4.4 \times 10^{-16}\,cm^2\,nm^4 \text{ for air} \right) .$$
(19.7)

Rayleigh phase fuction
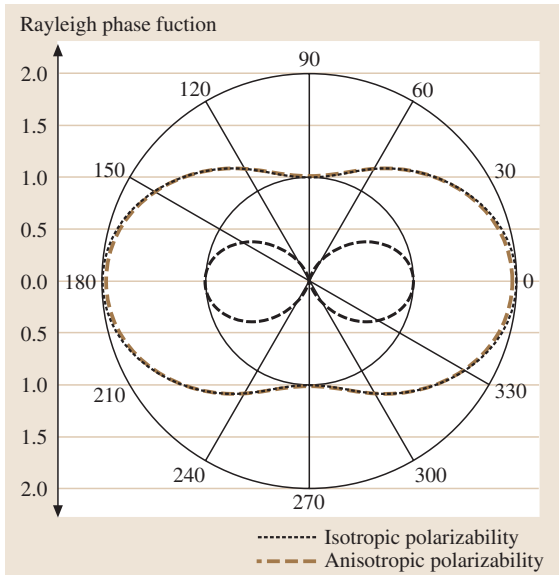
Fig. 19.1 Polar diagram of the Rayleigh scattering phase function $\Phi(\vartheta)$ for unpolarized incident light (*dashed line*, normalized to 2). The contribution of light polarized parallel to the scattering plane shows the $\sin^2 \vartheta'$ dependence of a Hertz dipole (*dotted line*, normalized to 1), with $\vartheta' = \pi/2 - \vartheta$ being the angle between dipole axis and the Poynting vector of the incident radiation, while the contribution of light polarized perpendicular to the scattering plane (*drawn line*, normalized to 1) is independent of ϑ. (plot by F. Filsinger)

The extinction coefficient due to Rayleigh scattering $\varepsilon_R(\lambda)$ is then given by

$$\varepsilon_R(\lambda) = \sigma_R(\lambda) N_{air} . \tag{19.8}$$

The Rayleigh scattering phase function (see Fig. 19.1) is given by

$$\Phi(\cos \vartheta) = \frac{3}{4}(1 + \cos^2 \vartheta) . \tag{19.9}$$

Taking the anisotropy of the polarisability into account the above equations becomes [19.3]:

$$\Phi(\cos \vartheta) = 0.7629(0.9324 + \cos^2 \vartheta) . \tag{19.10}$$

19.1.4 Raman Scattering

While Raman (and Mie) scattering can be regarded as elastic scattering processes, where no energy is transferred between the scattering particle and the photon, inelastic scattering occurs, if the scattering particle (i. e.

molecule) changes its state of excitation during the scattering process. A part of the photons energy is then passed from the photon to the molecule (Stokes lines, $\Delta J = +2$, S-branch) or vice versa (anti-Stokes, $\Delta J = 2$, O-branch). The term rotational Raman scattering (RRS) is used if only the rotational excitation is affected ($\Delta v = 0$). If the vibrational state also changes, the term (rotational-) vibrational Raman scattering (VRS) is used ($\Delta v = \pm 1$). Only discrete amounts of energy given by the difference between the discrete excitation states can be absorbed/emitted. For air (O_2 and N_2) RRS frequency shifts of up to $\pm 200 \, cm^{-1}$ occur, for VRS a vibrational shift of $\pm 2331 \, cm^{-1}$ for nitrogen and $\pm 1555 \, cm^{-1}$ for oxygen has to be added. The VRS is one order of magnitude weaker than the RRS, and RRS is roughly one magnitude weaker than Rayleigh scattering.

In the following we give a quantitative description of rotational- and vibrational-Raman scattering by O_2 and N_2 [19.4–7]. The scattered power density $I_{v, J \to v', J'}$ in [W/m^2] scattered into the full solid angle 4π involving a transition ($v, J \to v', J'$) is given by [19.8]:

$$I_{v, J \to v', J'}$$
$$= I_0 \sigma_{v, J \to v', J'} L N_{air} g_J (2J+1) \frac{1}{Z} e^{-E(v, J)/kT} , \tag{19.11}$$

where I_0 is the incident power density, N_{air} is the number of molecules in the scattering volume, L is the length of the volume and g_J is the statistical weight factor of the initial rotational state due to the nuclear spin; J and v are the rotational and vibrational quantum numbers, respectively. The factor $(2J+1)$ accounts for the degeneracy due to the magnetic quantum numbers while $\exp[-E(v, J)/kT]$ accounts for the population of the initial state of the molecule at temperature T. The state sum Z is given by the product of the rotational state sum Z_{rot} and the vibrational state sum Z_{vib}. The absolute cross section in (19.11) is given by $\sigma_{v, J \to v', J'}$, which can be obtained by integration of the differential cross section $d\sigma_{v, J \to v', J'}/d\Omega$ over the entire solid angle Ω. Note that the term differential refers to the solid angle. The energy of the molecule is characterized by the vibrational (v) and rotational (J) quantum numbers and given by

$$E(v, J) = E_{vib}(v) + E_{rot}(J)$$
$$= hc\tilde{v}\left(v + \frac{1}{2}\right) + hcBJ(J+1) , \tag{19.12}$$

assuming no coupling between rotation and vibration, B is the rotational constant and $\tilde{v}$ is the wave number in

cm^{-1} of the ground state vibration. Allowed transitions are, in that approximation, $\Delta J = 0, \pm 2$ resulting in the Q-, O- and S-branches and $\Delta v = 0, \pm 1$ for vibrational transitions. Due to the temperatures in the Earth's atmosphere only the ground vibrational state is occupied significantly, thus leading only to Stokes transitions of the vibrational states.

Polarization Properties of Vibrational Raman Scattered Light and Line Filling in

The polarization properties of isotropic and anisotropic component of Raman scattered light are described by (19.13), respectively:

$$\frac{I_{parallel}}{I_{perp}}(\text{anisotropic}) = \frac{6 + \cos^2 \Theta}{7} ,$$

$$\frac{I_{parallel}}{I_{perp}}(\text{isotropic}) = \cos^2 \Theta , \qquad (19.13)$$

where the terms parallel and perpendicular refer to the plane defined by the sun, the scattering point and the observer. Thus only the isotropic part leads to enhanced polarization of scattered light, especially at large scattering angles ($\approx$ solar zenith angle (SZA)). Since the Q-branch of the vibrational band of the Raman-scattered light consists of an isotropic fraction, this will lead to an enhanced degree of polarization in the centre of a Fraunhofer line. But due to the small cross section of vibrational Raman scattering, this enhancement is very small (e.g. $\cong 0.3\%$ for the Ca–I line at 422.7 nm and a resolution of 0.01 nm) and occurs only at large scattering angles. Thus the observed high degrees of polarization at small solar zenith angles cannot be attributed to vibrational Raman scattering [19.9].

Due to the relative small cross section of vibrational–rotational Raman scattering the additional filling in of Fraunhofer or terrestrial absorption lines is around 10% of the filling in due to rotational Raman scattering (see Table 19.1).

19.1.5 Mie Scattering

Mie scattering is (after [19.10]) defined as the interaction of light with (particulate) matter of dimensions comparable to the wavelength of the incident radiation. It can be regarded as the radiation resulting from a large number of coherently excited elementary emitters (i. e. molecules) in a particle. Since the linear dimension of the particle is comparable to the wavelength of the radiation, interference effects occur. The most noticeable difference compared to Rayleigh scattering is the usu-

Table 19.1 Comparison of the total cross section for the different scattering types for 770 nm, 273 K

Scattering type	Cross section (cm^2)	Ratio (%)
Rayleigh	1.156×10^{-27}	100
O$_2$ RRS	7.10×10^{-29}	6.1
N$_2$ RRS	2.94×10^{-29}	2.5
Air RRS	3.82×10^{-29}	3.3
VRS	–	0.1

ally much weaker wavelength dependence (see below) and a strong dominance of the forward direction in the scattered light. The calculation of the Mie scattering cross section can be very complicated (involving summing over slowly converging series), even for spherical particles, but even more so for particles of arbitrary shape. However, the Mie theory (for spherical particles) is well-developed and a number of numerical models exist to calculate scattering phase functions and extinction coefficients for given aerosol types and particle size distributions see Figs. 19.2, 19.17 [19.11, 12]. The computational effort is substantially reduced by the introduction of an analytical expression for the scattering phase function, which only depends on a few observable parameters. Most common is the Henyey–Greenstein parameterization:

$$\Phi(\cos \vartheta) = \frac{(1 - g^2)}{4\pi(1 + g^2 - 2g \cos \theta)^{3/2}} , \qquad (19.14)$$

which only depends on the asymmetry factor g (average cosine of the scattering function):

$$g = \langle \cos \theta \rangle = \frac{1}{2} \int_{-1}^{1} P(\cos \theta) \cos \theta \, d \cos \theta \qquad (19.15)$$

see e.g. [19.11]. For isotropic scattering [$\Phi(\cos \theta) = $ const] the asymmetry factor $g = 0$ while for a tropospheric aerosol a typical value might be as large as $g \approx 10$.

Tropospheric aerosol is either emitted from the surface (e.g. sea salt, mineral dust, biomass burning) or forms in the gas phase by condensation of chemically formed hygroscopic species (primarily sulphates, nitrates, or oxidized organic material). The aerosol load of the atmosphere, i. e. particle number density and size distribution, depends on the aerosol origin and history. Parameters for typical aerosol scenarios (urban, rural, maritime, background) can be found in the database for the radiative transfer model LOWTRAN [19.13], which includes the extinction coefficients and the asymmetry

factors as well as their spectral dependence. Another important aspect is Mie scattering by cloud particles. A radiative transfer model including all cloud effects known to date was, e.g., developed by *Funk* [19.14].

Mie scattering is only partly an absorption process, but by similar arguments as in the case of Rayleigh scattering, for narrow beams it can be treated as an absorption process with an extinction coefficient of

$$\varepsilon_M(\lambda) = \varepsilon_{M0}\lambda^{-\alpha} \qquad (19.16)$$

with the Angström exponent α being inversely related to the mean aerosol particle radius. Typically α is found to be in the range 0.5–2.5 with an average value of $\alpha = 1.3$ [19.15, 16]. For the ideal case of an exponential aerosol size distribution:

$$\frac{\Delta N}{\Delta r} = r^{-(\nu+1)} .$$

The Angström exponent is related to the Junge index ν by $\nu = \alpha + 2$ [19.17]. Thus an Angström exponent of 1.3 would correspond to a Junge index of 3.3.

In summary a more comprehensive description of atmospheric extinction (in the presence of a single trace gas species and neglecting Raman scattering) can be expressed as:

$$I(\lambda) = I_0(\lambda)\exp\left\{-L[\sigma(\lambda)c + \varepsilon_R(\lambda) + \varepsilon_M(\lambda)]\right\} . \qquad (19.17)$$
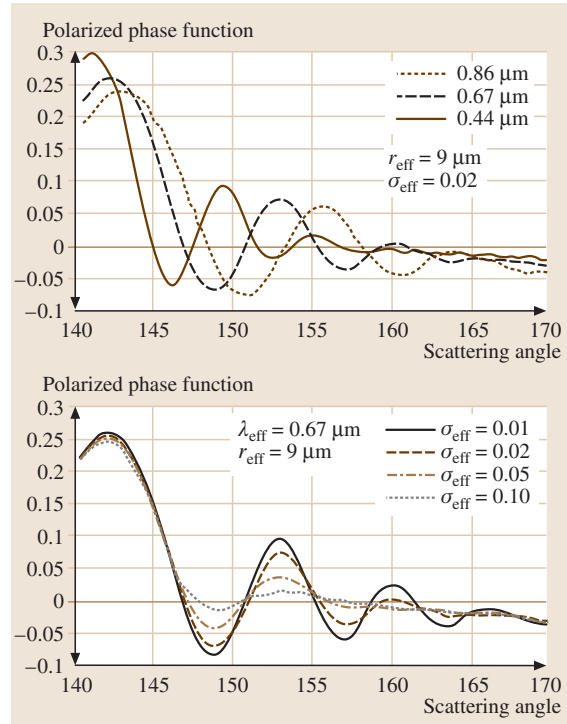
Typical extinction coefficients due to Rayleigh and Mie scattering at 300 nm are 1.3×10^{-6} cm^{-1} and 1–10×10^{-6} cm^{-1}, respectively.


Fig. 19.2 Polarized Mie scattering phase function as a function of scattering angle for cloud droplet having a lognormal particle size distribution with an effective radius $r_{eff} = 9\,\mu m$. *Upper panel*: phase function as a function of wavelength with fixed $\sigma_{eff} = 0.02$ effective size variance; *lower panel*: as a function of effective size variance (courtesy of *Bréon* and *Goloub*, 2003)

19.2 The Radiation Transport Equation

In this section we present the basic equations describing the radiation transport (RT) in absorbing and scattering media as described by the above elementary processes. In physical notation the RT equation is a continuity equation with corresponding source and sink terms (Fig. 19.3); these source and sink terms are assumed to be linear in the radiant flux Φ, intensity I, or radiance F (19.1, 19.3, 19.4).

19.2.1 Sink Terms (Extinction)

First we consider the radiant flux Φ per unit space angle Ω and wavelength λ i.e., the incoming intensity I_λ (19.3) which is attenuated within the distance

ds by absorption and scattering. As before we refer to the absorption (a) and scattering (s) coefficients with $\varepsilon_a = N\sigma_a(\lambda)$ and $\varepsilon_s = N\sigma_s(\lambda)$, respectively, with N being the number of absorber or scatterers per volume and $\sigma_i(\lambda)$ being absorption or scattering cross sections. Both processes are commonly referred to as extinction. Accordingly, we obtain the following continuity equation for the incoming intensity traversing the distance ds

$$dI_\lambda = -[\varepsilon_a(\lambda) + \varepsilon_s(\lambda)]I_\lambda\,ds$$
$$= -[\sigma_a(\lambda) + \sigma_s(\lambda)]nI_\lambda\,ds , \qquad (19.18)$$

where ε_a is the absorption coefficient, ε_s is the scattering coefficient, $\sigma_a(\lambda)$ is the absorption cross section of the
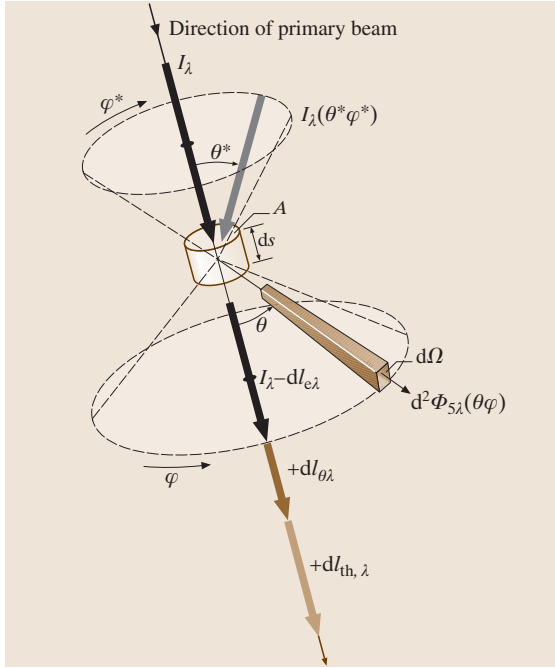
Fig. 19.3 Schematic drawing of the continuity equation for radiative transfer. The continuity assumes linearity of processes in the intensity I_λ. When passing through a distance ds the incoming radiation I_λ is attenuated by extinction (absorption and scattering), $I_{e,\lambda}$. The source term for the outgoing light is the scattered light $dI^*_{s,\lambda}$ from the space angles θ^* and φ^* and thermal radiation $dI^*_{th,\lambda}$ (courtesy of Rödel, 1999)

absorber (molecule), $\sigma_s(\lambda)$ is the scattering cross section of the absorber (molecule), and n is the number of absorbers per unit volume.

19.2.2 Source Terms (Scattering and Thermal Emission)

In the gas phase there are two sources of radiation: thermal emission and scattering, i. e. the radiation removed from the primary beam due to scattering (19.18) reappears as a radiation source.

Scattering
Evidently, the outgoing light receives some intensity $dI^*_{s,\lambda}$, by scattering from all space angles θ^* and φ^*. We introduce a dimensionless scattering function $S(\theta^*, \varphi^*)$

$$S_\lambda(\theta, \varphi) = \frac{4\pi}{\sigma_s} \frac{d\sigma_s(\lambda)}{d\Omega} \tag{19.19}$$

which we integrate over all angles weighted with the incoming intensity $I^*_s, \lambda(\theta^*, \varphi^*)$

$$dI^*_s(\lambda) = \varepsilon_s(\lambda)\,ds \int_0^\pi \int_0^{2\pi} I^*(\lambda, \theta^*, \varphi^*)$$
$$\times \frac{S(\theta^*, \varphi^*)}{4\pi} \, d\varphi^* \sin\theta^* \, d\theta^* \tag{19.20}$$

to obtain the intensity added to the outgoing intensity dI^*_s.

Thermal Emission
Finally the intensity due to thermal emission $dI_{th}(\lambda, T)$ by the volume element ($dV = A\,ds$) is added to the outgoing intensity

$$dI_{th}(\lambda, T) = \varepsilon_a(\lambda)I_p(\lambda, T)\,ds = \varepsilon_a(\lambda)F_p(\lambda, T)A\,ds \tag{19.21}$$

where, as before, K_a denotes the absorption coefficient and $F_P(\lambda, T)$ denotes the Planck function

$$dF_P(\lambda, T) = \frac{2hc^2}{\lambda^5} \frac{d\lambda}{e^{hc/\lambda kT} - 1} . \tag{19.22}$$

Combining the above source and sink terms we obtain the radiation transport equation (19.23):

$$\frac{dI(\lambda)}{ds}$$
$$= -[\varepsilon_a(\lambda) + \varepsilon_s(\lambda)]I(\lambda) + \varepsilon_a(\lambda)I_P(\lambda, T) + \varepsilon_s(\lambda)$$
$$\times \int_0^\pi \int_0^{2\pi} I^*(\lambda, \theta^*, \varphi^*) \frac{S(\theta^*, \varphi^*)}{4\pi} \, d\varphi^* \sin\theta^* \, d\theta^* \tag{19.23}$$

19.2.3 Simplification of the Radiation Transport Equation

Frequently simplifications of the radiation transport equation are possible, if only partial systems are of interest.

For instance at short wavelengths (UV, visible) the Planck term can usually be neglected:

$$\frac{dI(\lambda)}{ds} = -[\varepsilon_a(\lambda) + \varepsilon_s(\lambda)]I(\lambda) + \varepsilon_s(\lambda)$$
$$\times \int_0^\pi \int_0^{2\pi} F(\lambda, \theta, \varphi) \frac{S(\theta, \varphi)}{4\pi} \, d\varphi \sin\theta \, d\theta . \tag{19.24}$$

If thermal radiation (from the atmosphere) is of interest due to its long wavelength, Rayleigh and Mie scattering

(by aerosol particles and cloud droplets) can frequently be neglected

$$\frac{dI(\lambda)}{ds} = \varepsilon_a(\lambda)[AF_P(\lambda, T) - I(\lambda)] \,. \qquad (19.25)$$
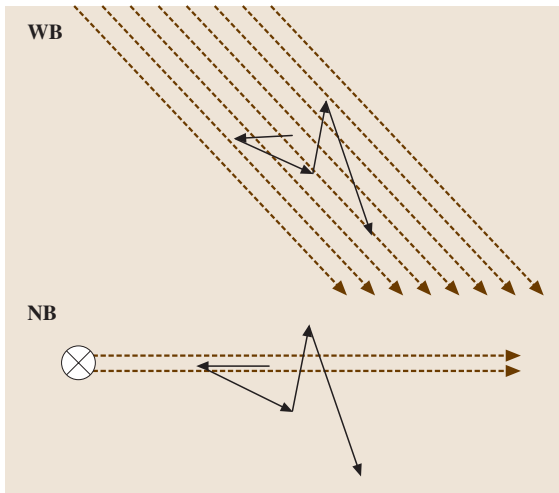
With the definition of the optical density $d\tau = \varepsilon_a(\lambda) ds$ and after division by A the above equation becomes

$$\frac{dF(\lambda)}{d\tau} = F_P(\lambda, T) - F(\lambda) \,. \qquad (19.26)$$

This latter equation is also known as the Schwarzschild equation.

19.2.4 Light Attenuation in the Atmosphere

When considering the question of the attenuation of radiation in the atmosphere, two (extreme) cases can be distinguished, as illustrated in Fig. 19.4: wide beams (WB, as e.g. the illumination of the Earth's atmosphere by the sun) and narrow beams (NB, as e.g. the light beam emitted by a searchlight-type differential optical absorption spectroscopy (DOAS) light source).

Wide Beams (WB) in the Atmosphere: The Two-Stream Model

In the following we consider the transport of solar radiation in the atmosphere. Compared to the general form of the radiation transport equation (19.23) the problem is simplified by assuming a flat, horizontally homogeneous and infinite atmosphere. Therefore only the vertical (z) component of the radiance has to be considered.

When radiation enters the atmosphere from above, its vertical component is counted as 'downwelling radiation' $F_\downarrow(\lambda, z)$; upon interaction with atmospheric constituents (gases or aerosol) this radiation is either absorbed or scattered (Fig. 19.5). These extinction processes reduce the amount of downwelling radiation (according to (19.17) where the extension of the light path for non-vertical rays has to be taken into account). While the absorbed radiation causes no further problems, the scattered radiation appears as a source term, which is split into two parts (taking the phase function into account): A downwelling part, which adds to $F_\downarrow(\lambda, z)$ and an upwelling part, which is added to a second, upwelling radiation flux $F_\uparrow(\lambda, z)$. Thermal emission adds to both, $F_\downarrow(\lambda, z)$ and $F_\uparrow(\lambda, z)$. For practical calculation the atmosphere is divided into layers of thickness dz, which change the
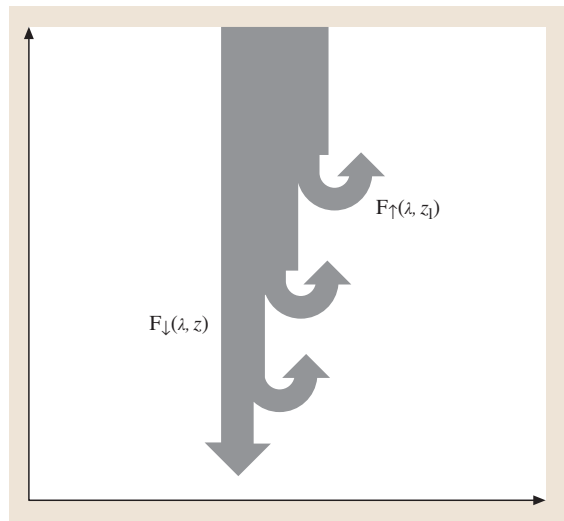

Fig. 19.4 Difference between Wide Beams (WB, *top*) as, e.g., the illumination of the Earth's atmosphere by the sun, and Narrow Beams (NB, *bottom*) as, e.g., the light beam emitted by a searchlight-type light source. In the NB case the probability of a photon being scattered back into the beam after being scattered out of the beam is generally negligible, therefore extinction can be treated like absorption. In the case of a WB the lateral (i. e. perpendicular to the propagation of the incident radiation flux) radiation flux can be neglected. Therefore the scattering has only the effect of reflecting some of the incoming light, as can be calculated by, e.g., a two-stream model (see above)

Fig. 19.5 The two-stream model. In a horizontally homogeneous atmosphere radiation transport can be represented by just two 'streams of radiation', the downwelling flux and the upwelling flux

radiance F traversing it by dF. The net radiance is composed of both components (up- and downwelling radiances)

$$F_n(\lambda, z) = F_\uparrow(\lambda, z) - F_\downarrow(\lambda, z) . \qquad (19.27)$$

Narrow Beams (NB) in the Atmosphere

In the case of a WB the lateral (i. e. perpendicular to the propagation of the incident radiation flux) radiation flux can be neglected. Therefore the scattering has only the effect of reflecting some of the incoming light, as can be calculated by e.g. a two-stream model (see above).

In contrast, in the case of narrow beams the probability of a photon being scattered back into the beam after being scattered out of the beam is generally negligible (Fig. 19.4), therefore extinction can be treated as absorption.

The attenuation of a light beam by extinction due to atmospheric constituents is in principle described by (19.17). For practical purposes of measurements in the atmosphere, however, (19.17) is oversimplified in that it neglects the presence of other causes of light extinction, including absorption by other molecules present in the atmosphere.

In the natural atmosphere many different molecular species will absorb light. Equation (19.17) must therefore be further extended to

$$I(\lambda) = I_0(\lambda) \exp\left(-L\{\Sigma[\sigma_i(\lambda)c_i] + \varepsilon_R(\lambda) + \varepsilon_M(\lambda)\}\right) , \qquad (19.28)$$

where $\sigma_i(\lambda)$ and c_i denote the absorption cross section and the concentration of the i-th species, respectively.

19.3 Aerosols and Clouds

Aerosols are a natural constituent of the Earth's atmosphere and their origin is mostly natural, although lately the anthropogenic contribution is increasing. An aerosol is defined as a stable suspension of particles, liquid or solid, in a carrier gas like atmospheric air. Therefore dust, haze, smoke, smog, fog, mist, and clouds can be considered to be specific aerosol types. The total mass of natural aerosols was found be four times larger than due to human activity in 1968, and by the year 2000 the anthropogenic contribution is estimated to have doubled. According to *Junge* and *Manson* [19.18], aerosols can be classified by sizes: particles with diameters below 0.1 mm are named Aitken particles, while those with sizes between 0.1–1 mm are "large" particles, and those larger than 1 mm are called "giant" particles. The aerosols may also be classified according to their origin into marine, continental, rural, remote, background, and urban aerosol, where each category has different characteristics like chemical composition, size distribution, shapes and so on. Aitken nuclei, i. e. the smallest atmospheric aerosol particles, are naturally produced from supersaturated vapors by a process called gas-to-particle conversion (GPC), often in connection with photochemical reactions between gas-phase constituents (Fig. 19.6). Anthropogenic activities such as combustion and industrial processes increasingly lead to the release of aerosol particles, or precursor gases from which aerosol particles are formed, into the atmosphere. Large aerosol particles can be produced by combustion processes and other an-

thropogenic or natural processes (e.g. the coagulation of smaller Aitken nuclei). Natural sources for giant particles are bulk-to-particle conversion (BPC) processes like sea-salt aerosol production, or desert dust mobilization, while human activity contributes, for example through emission from industries, mining, biomass and wood burning, and agricultural dust generation.

In the atmosphere, typical particle number concentration decreases with increasing particle size since Aitken particles are newly produced; they subsequently coagulate and form fewer larger particles. Accordingly Aitken particles usually dominate the total number of particles in an air sample, but their contribution to the total aerosol volume is small, whilst an increasing contribution is due to the large and giant particles. Conversely, Aitken particles often dominate the surface available for heterogeneous reactions. For particles with sizes ranging from a few nanometers up to tens of micrometers typical number concentrations can be coarsely specified. For example, typical aerosol numbers are: 1) $\approx 1.4 \times 10^4\,\text{cm}^{-3}$ at the (continental) ground level total concentrations, 2) $\approx 6 \times 10^2\,\text{cm}^{-3}$ in remote continental regions, 3) $10^5\,\text{cm}^{-3}$ in large cities, 4) $\approx 3 \times 10^4\,\text{cm}^{-3}$ in small towns, 5) $\approx 5 \times 10^2\,\text{cm}^{-3}$ over remote oceans, 6) $\approx 50\,\text{cm}^{-3}$ in the clean Arctic, and 7) even lower in the remote Antarctica. The vertical aerosol profiles (in number of particles per cubic centimeter of air) frequently show an exponential decay for the lowest 6 km of the atmosphere. Above
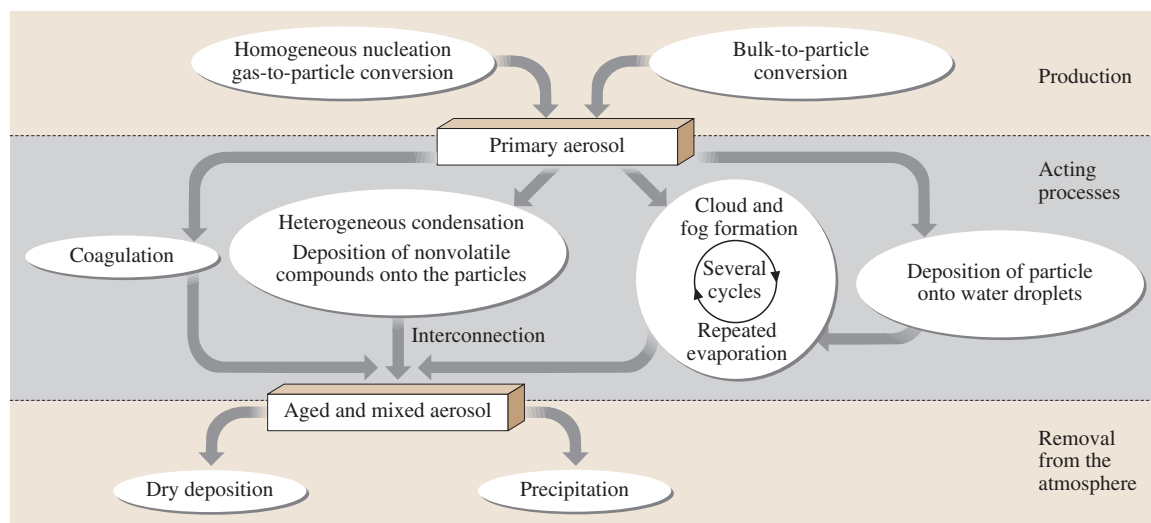
Fig. 19.6 Aerosol-related processes in the atmosphere involving particle formation, processes altering particle characteristics, and removal from the atmosphere

this level, background tropospheric aerosol concentrations (in the Aitken mode) are around $200-300$ particles per cm^3. Above the tropopause up to around $30\,km$, the total number concentration decreases again to a minimum below $1-10\,cm^{-3}$ particles in volcanically quiet periods and $1000\,cm^{-3}$ after major volcanic eruptions.

At any time, about 50% of the globe is cloud covered. Atmospheric clouds are volumes of water-supersaturated air containing hydrometeors, which are microscopic objects (e.g. aerosol particles, cloud droplets, ice and snow crystals) as well as macroscopic objects (snowflakes, graupel grains, raindrops, and hailstones). The individual cloud particles have sizes with radii ranging from $0.001\,mm$ to several hundreds of micrometers, or even centimeters, as in the case of hailstones.

Atmospheric clouds can be classified into four major categories: 1) low-level cloud in the lower troposphere ($< 2.5\,km$), 2) middle-level clouds in the middle troposphere ($2.5-8\,km$), 3) higher clouds in the upper troposphere ($8-15\,km$), and 4) middle (stratospheric) and upper (mesospheric) atmospheric clouds, which themselves form 11 major subgroups (1.1 cumulus, 1.2 stratocumulus, 1.3 stratus, 2.1 altocumulus, 2.2 altostratus, 2.3 nimbostratus, 3.1 cirrus and cirrostratus, 3.2 cirrocumulus, 3.3 cumulonimbus, 4.1 polar stratospheric clouds, and 4.2 noctilucent clouds) of some 100 different cloud types in total.

Both aerosols and clouds have a considerable impact on atmospheric photochemistry and radiation. Their effects in atmospheric photochemistry are most noticeably in: 1) the heterogeneous processing of longer-lived and ozone-friendly halogen species ($ClONO_2$, HCl, $BrONO_2$,...) into ozone-harmful halogen oxides (ClO, BrO) on polar stratospheric cloud particles, which is a major reason for the formation of the Antarctic ozone hole, 2) uptake of acids (e.g., H_2SO_4, HNO_3, HCl, HBr,...) and of N_2O_5 on the stratospheric or tropospheric aerosols and cloud particles, 3) in the heterogeneous conversion of SO_2 into H_2SO_4, or NO_3 and N_2O_5 into HNO_3 and 4) the uptake of species such as NH_3HNO_3, or NH_4HSO_4 into atmospheric aerosols and cloud particles. Eventually when these particles grow large enough ($>$ some μm), the respective gases attached or solved inside are efficiently washed out from the atmosphere.

Aerosols and clouds also have a large effect on the radiative budget of the atmosphere, primarily by increasing the scattering of the incoming solar and outgoing thermal radiation. Clouds affect radiation both through their three-dimensional geometry and the amount, size and nature of the hydrometeors which they contain. In climate models these properties translate into cloud cover at different levels, cloud water content (for liquid water and ice) and cloud droplet (or crystal) equivalent radius. The interaction of clouds and radiation also involves other parameters (asymmetry factor of the Mie diffusion) which depend on cloud composition, and most notably on their phase.

In effect, the occurrence of aerosols and clouds increases the planetary albedo A of the solar short-wave (SW) radiation, and thus lead to a net cooling of the Earth. Conversely clouds, and to a much lesser degree aerosols, increase the infrared albedo B of the atmosphere and thus increase the downwelling atmospheric long-wave (LW) radiation which increases the surface temperature. The subtle balance between cloud impact on the SW and terrestrial long-wave radiation altered by a change in any of the aforementioned parameters, the dependence of the radiation budget on altitude at which clouds occur and the solar inclination (latitude and season) make clouds the most sensitive factors to affect the global climate in both directions (cooling/warming).

19.4 Radiation and Climate

The atmospheric radiation budget largely determines the Earth's climate. Evidently the incoming solar or short-wave (SW) radiation shining on the globe has to be balanced by the outgoing long-wave (LW) radiation. This thermal equilibrium between incoming SW and outgoing LW radiation and can be simply expressed by

$$S_0(1 - A)/4 = \varepsilon(1 - B)\sigma T_s^4 \qquad (19.29)$$

where S_0 is the solar constant ($1370\,\text{W/m}^2$), A is the terrestrial SW albedo (0.298), the factor 4 coming from geometric considerations, ε is the LW emissivity (0.96), B is the atmospheric LW albedo (0.34), σ is Boltzmann's constant ($5.67 \times 10^{-8}\,\text{W/m}^2/\text{K}$), and T_s is the average temperature ($T_s = 286\,\text{K}$) of the Earth's surface. It thus becomes clear that the globe's surface temperature T_s is given by a delicate balance of the parameters S_0, A, and B. In geological and historic

Table 19.2 Compendium of change in recognized periods in climate change and changes in the solar constant S_0

| Time scale/period	Cause	Change in solar constant S_0	Observation/problem
4.5 Ga	Secular trend in solar output	Secular 25–30% increase	'Faint Sun problem', i. e. liquid H_2O should not have been there, but was present since 4 Ga before present
450 ka	Change in orbital eccentricity $\Delta\varepsilon = 0.06$	$< 0.7\,\text{W/m}^2$ (Milankovitch)	Change in ice volume, $\Delta^{18}O/^{16}O$ in H_2O and $CaCO_3$ in foraminifera
100 ka	Change in orbital eccentricity $\Delta\varepsilon = 0.06$	$< 0.7\,\text{W/m}^2$ (Milankovitch)	Change in ice volume, $\Delta^{18}O/^{16}O$ in H_2O and $CaCO_3$ in foraminifera
41 ka	Change in obliquity (axial tilt) due to Earth and Jupiter's orbital plane tilt	June insulation changed by 25% at 80°N, no net change on annual S_0 (Milankovitch)	Change in ice volume, $\Delta^{18}O/^{16}O$ in H_2O and $CaCO_3$ in foraminifera
23 ka		June insulation changed by $100\,\text{W/m}^2$ at 60° N, no net change on annual S_0 (Milankovitch)	Change in ice volume, $\Delta^{18}O/^{16}O$ in H_2O and $CaCO_3$ in foraminifera
1.5 ka	Unclear whether cause is solar, 'eigenmode' of the climate system?		^{14}C and ^{10}Be variation in oceanic sediments, ^{14}C variation in tree rings
210a (Suess) 148a, and 88a (Gleisberg) cycles	Unclear whether cause is solar, 'eigenmode' of the climate system?		^{14}C variation in tree rings, ^{14}C and ^{10}Be variation ice cores,
22a	Sun spot 'overtone', eigenmode in solar magnetic field oscillation	$\Delta S_0 \approx 1.5\,\text{W/m}^2$, UV radiation changes by 0.37–0.6%	Change in atmospheric circulation?
11a (Schwabe 1843)	Sun spot 'overtone', eigenmode in solar magnetic field oscillation		Change in atmospheric circulation?
4w (27d)	Sun rotation period	Small	?

Fig. 19.7a–c Schematic overview of the SW (*left part*) and LW (*right part*) radiative transfer in the atmosphere; *upper panel*: **(a)** incoming solar SW and outgoing LW terrestrial spectrum, **(b)** atmospheric absorption from individual gases at ground level (total atmosphere) and **(c)** at 11 km

times, the solar constant is known to have varied on different timescales, mostly given by changes in the Earth's orbital parameters, as suggested by *Milankovitch* in 1941 [19.19] and solar activity (Table 19.2), causing well recognized and significant effects on the Earth's climate. In this context, most notable is that the size ΔS_0 of any of the known processes listed in Table 19.2 has not been sufficiently large to be held solely responsible for documented ΔT_s changes, which were inferred to be as large as some 10 °C. Therefore, it is well accepted that the global climate system amplifies external disturbances (forcing) through interacting complicated positive and negative feedback cycles (Table 19.2).

Another factor important for T_s is of course the magnitude and variability of the SW albedo A (19.35). This is largely influenced by the amount of cloud and the abundance of atmospheric aerosol; the latter is either due to increasing directly back reflection of SW radiation to space, or by altering the cloud particle formation processes, a process called the indirect aerosol effect [19.20, 21]. In the recent past changes in the global albedo due to increasing atmospheric aerosol abundances, mostly particles containing sulphuric acid has been well recognized and held partly responsible for lower global T_s between the late 1940s to late
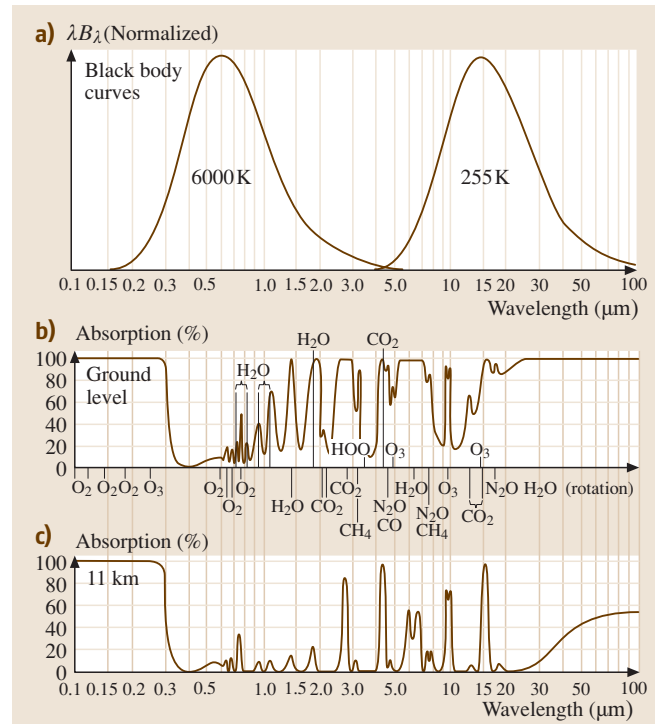
1970s [19.20]. Changing global cloud cover is also likely to have occurred in the past. In the tropics, which are a particularly sensitive region for the global energy budget, the cloud cover appears to be highly variable on timescales ranging from days to decades. Accordingly, satellite-based cloud cover records that began in the late
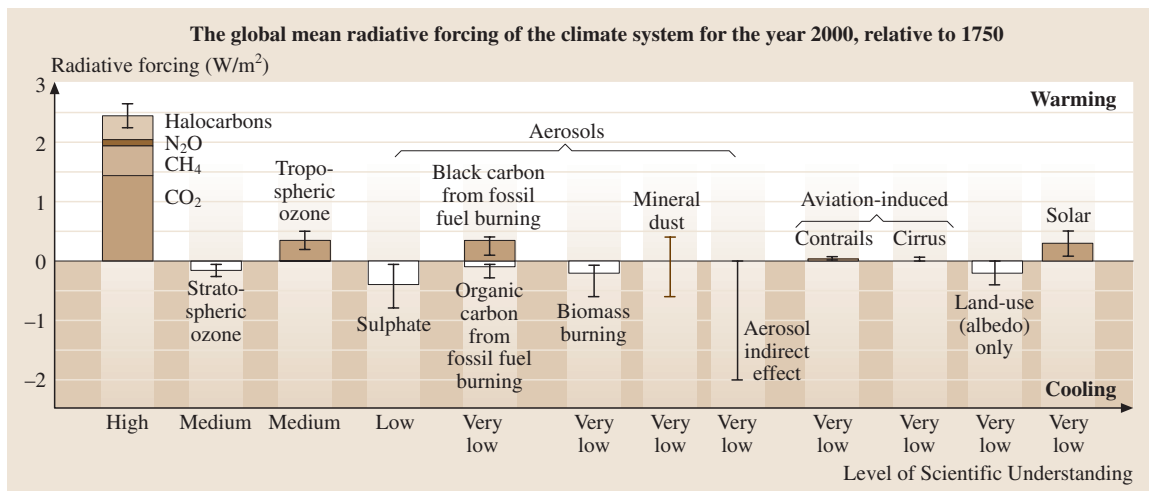
Fig. 19.8 External factors which force climate change (adopted from IPCC, 2001)

1970s are still insufficiently long to establish unambiguously an observation-based relation between a changing A and T_s [19.22].

The atmospheric LW albedo B is responsible for the greenhouse effect of the atmosphere. If B were zero, then according to (19.35), T_s would be 255 K, clearly cooler than the habitable Earth is able to provide ($T_s = 287$ K). The value of B is due to the combined action of the most important atmospheric greenhouse gases H_2O, CO_2, CH_4, O_3, N_2O, and many others, mostly man-made, trace molecules [19.20]. It appears that, even though each greenhouse gas has its own specific spectrum, they combine in a way that only a small fraction of the outgoing LW radiation is not absorbed in the atmosphere, i. e., radiation in the atmospheric window (8–14 μm) (Fig. 19.7).

In 1896, the atmospheric greenhouse effect of CO_2 was already recognized by S. Arrhenius. Accordingly it is undisputed in the scientific community that rising atmospheric CO_2 concentrations affect the atmospheric LW budget and thus T_s. Radiative transfer calculations show that the CO_2 increase from preindustrial 280 ppm to presently 370 ppm alone gives rise to a present radiative forcing of 1.4 W/m^2 and for all greenhouse gases of 2.4 W/m^2 ([19.20], Fig. 19.8). Naively adding the respective radiative forcing in (19.18) leads to a $\Delta T_s = +0.7$ K, precisely the value that is reported for the global average temperature rise in the past 150 y [19.20]. However, due to the complicated interactions in the climate system, it is disputed how the global climate system is and will react in detail to future man-induced LW radiative forcing.

19.5 Applied Radiation Transport: Remote Sensing of Atmospheric Properties

19.5.1 Trace Gases

Measurements of trace gas concentrations (and other quantities such as aerosol distribution or the intensity of the radiation field in the atmosphere) are the experimental prerequisites for the understanding of the physico-chemical processes in the Earth's atmosphere. At the same time the determination of trace gas concentrations in the atmosphere constitutes a challenge for the analytical techniques employed in several respects: It is well known (e.g. *Perner* et al. [19.23]) that species (such as OH radicals) present at mixing rations ranging from as low as 0.1 ppt (one ppt corresponds to a mixing ratio of 10^{-12}, equivalent to about 2.4×10^7 molecules/cm^3) to several ppb (1 ppb corresponds to a mixing ratio of 10^{-9}) can have a significant influence on the chemical processes in the atmosphere. Thus, detection limits from below 0.1 ppt to the ppb range are required, depending on the application. On the other hand, measurement techniques must be specific, i. e. the result of the measurement of a particular species should neither be positively nor negatively influenced by any other trace species simultaneously present in the probed volume of air. Given the large number of different molecules present at the ppt and ppb level, even in clean air, meeting this requirement is also not trivial.

Presently many highly sophisticated techniques for the measurement of atmospheric trace species are in use. Among these, spectroscopic techniques [19.24, 25] offer a series of unique advantages including high (i. e. ppt-level in many cases) sensitivity, very specific detection of a given molecule, inherent calibration, and wall-free operation. These properties, in combination, are difficult to obtain in techniques based on other principles. Here we describe a particular technique, differential optical absorption spectroscopy (DOAS), which has been successfully used in atmospheric measurements for several decades now, while new applications continue to be introduced.

19.5.2 The Fundamentals of DOAS

The DOAS technique [19.26, 27] makes use of the structured absorption of trace gases. Typically spectra are recorded which encompass several hundred spectral channels. Evaluation is done by fitting the spectral structure of the trace gases, thus making use of all the spectral information. DOAS has proven to be particularly useful for the determination of the concentration of unstable species such as free radicals or nitrous acid. In addition, the abundance of aromatic species can be determined at high sensitivity (see below). DOAS, like all spectroscopic techniques, relies on the absorption of electromagnetic radiation by matter. Quantitatively the absorption of radiation is expressed by the Lambert–Beers law:

$$I(\lambda) = I_0(\lambda) \exp[-L\sigma(\lambda)c] , \tag{19.30}$$

where $I(\lambda)$ is the intensity after passing through a layer of thickness L, while $I_0(\lambda)$ denotes the initial intensity emitted by the light source. The species to be measured is present at the concentration (number density) N_c. The quantity $\sigma(\lambda)$ denotes the absorption cross section at the wavelength λ; it is a characteristic property of any species. The absorption cross section $\sigma(\lambda)$ can be measured in the laboratory, while the determination of the light path length L is trivial in the case of the arrangement of an artificial light source and detector (Fig. 19.9, arrangement a). Once those quantities are known, the trace gas concentration c can be calculated from the measured ratio $I_0(\lambda)/I(\lambda)$. In contrast to laboratory spectroscopy, the true intensity $I_0(\lambda)$, as would be received from the light source in the absence of any absorption, is usually difficult to determine when measurements are made in the open atmosphere or in smog chambers. The solution lies in measuring the so-called differential absorption. This quantity can be defined as the part of the total absorption of any molecule rapidly varying with wavelength and is readily observable, as will be shown below. Accordingly, the absorption cross section of a given molecule (numbered i) can be split into two portions:

$$\sigma_i(\lambda) = \sigma_{i0}(\lambda) + \sigma_i'(\lambda) , \qquad (19.31)$$
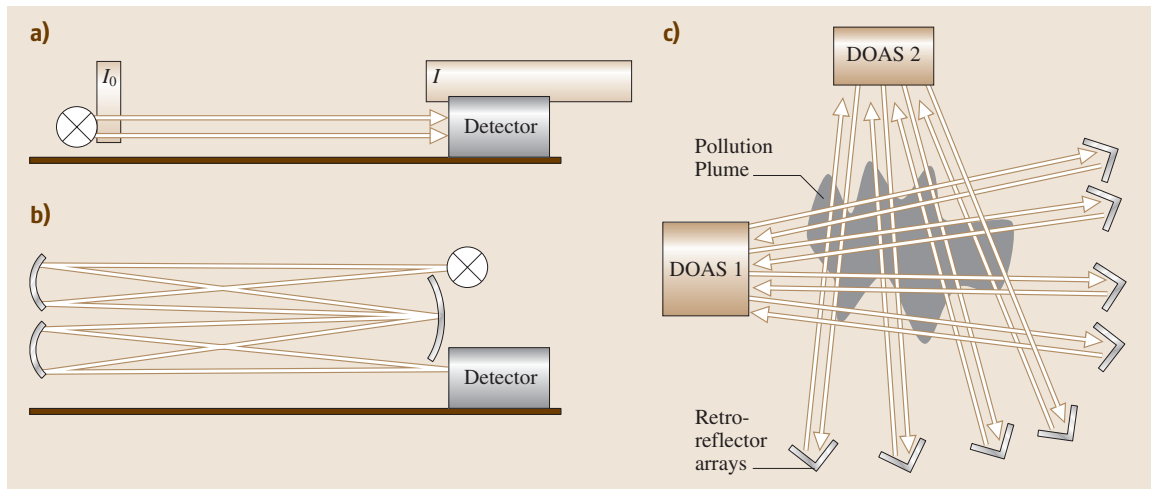
where $\sigma_{i0}(\lambda)$ varies only slowly with the wavelength λ, for instance describing a general slope, while $\sigma_i(\lambda)$

shows rapid variations with λ, for instance due to an absorption line. The meaning of rapid and slow (or rather smooth and structured) variation of the absorption cross section as a function of wavelength is, of course, a question of the observed wavelength interval and the width of the absorption bands to be detected. Note that extinction due to Rayleigh and Mie scattering can be assumed to be slowly varying with λ. Thus (19.30) becomes

$$
\begin{aligned}
I(\lambda) = {} & I_0(\lambda) \exp\left\{-L\Sigma\left[\sigma_i'(\lambda)N_{ci}\right]\right\} \\
& \times \exp\left(-L\{\Sigma[\sigma_{i0}(\lambda)c_i] + \varepsilon_R(\lambda) + \varepsilon_M(\lambda)\}\right) \\
& \times A(\lambda) , \qquad (19.32)
\end{aligned}
$$

where the first exponential function describes the effect of the structured, differential absorption of trace species, while the second exponential constitutes the slowly varying absorption of atmospheric trace gases as well as the influence of Mie and Rayleigh scattering described by the extinction coefficients $\varepsilon_R(\lambda)$ and $\varepsilon_M(\lambda)$, respectively. The attenuation factor $A(\lambda)$ describes the (slow) wavelength-dependent transmission of the optical system used. Thus we can define a quantity I_0' as the intensity in the absence of differential absorption:

$$
\begin{aligned}
I_0'(\lambda) & \\
= {} & I_0(\lambda) \times A(\lambda) \\
& \times \exp\left(-L\{\Sigma[\sigma_{i0}(\lambda)N_{ci}] + \varepsilon_R(\lambda) + \varepsilon_M(\lambda)\}\right) . \\
& \qquad (19.33)
\end{aligned}
$$

Fig. 19.9a–c The active DOAS principle can be applied in several light-path arrangements and observation modes using artificial light sources such as arc lamps or incandescent lamps in a searchlight-type arrangement, or lasers. The light-path-averaged trace gas concentration is determined in the 'traditional' setup **(a)**. In situ concentrations are measured with multiple reflection cells **(b)**. The new 'tomographic' arrangement **(c)** employing many DOAS light paths allows mapping of (two- or three-dimensional) trace gas distributions

Fortunately the effect of slowly varying absorbers, i. e. the exponential in (19.33), can be removed by high-pass filtering the spectral data, thus only the first exponential function in (19.32) remains, which is essentially Lambert–Beers law [(19.30) for more than one absorber]. It should be noted that the length of the light path is more difficult to determine – or might actually not have a precise meaning – in applications where direct or scattered sunlight is used (arrangements d, e, and f and Fig. 19.11), in this case the column density S of the trace gas

$$S = \int_0^\infty N_c(l)\,dl \qquad (19.34)$$

can still be determined. In the case of a constant trace gas concentration $N_{c_0}(l) = c_0$ along a path length L the column density simply becomes $S = N_{c_0}L$.

In order to obtain sufficient sensitivity, light-path lengths L of the order of several 100 m to several 1000 m are usually required. For measurements in the free atmosphere, assuming the arrangement a in Fig. 19.9, the trace gas concentration is averaged over the whole length of the light path, which makes the measurement less susceptible to local emissions. On the other hand measurements must frequently be made in a small volume (e.g. in photo-reactors); in these cases multi-reflection

systems can be used to fold the light path into a small volume [19.28]. An example of detection limits attainable with multi-reflection systems is given in Table 19.3.

19.5.3 Variations of DOAS

The DOAS technique can be adapted to a large variety of measurement tasks; as a consequence there are many variants of the DOAS technique in use. These can be grouped into active techniques, which employ their own light sources (e.g. Xe-arc lamps or incandescent lamps), and passive techniques, which rely natural light sources (e.g. sunlight, moonshine or starlight).

The most common active DOAS light-path arrangements include (Fig. 19.9):

a) The traditional active long-path systems (usually folded once);
b) Active systems using multi-reflection cells (e.g. white cells);
c) Recently the first tomographic systems allowed the determination of 3-D trace gas distributions by multiple-beam active DOAS.

The most common passive DOAS light path arrangements include (Fig. 19.10):

d) Zenith scattered light (ZSL)-DOAS is well-suited to study stratospheric trace gases. For instance a global network of ZSL-DOAS instruments continuously watches the distribution of stratospheric species (e.g. O_3, NO_2, BrO, OClO).
e) Multi-AXis (MAX)-DOAS allows determination of trace gases and their vertical distribution in e.g. the atmospheric boundary layer or the detection of plumes from cities, stacks, or volcanoes. In addition Airborne Multi-AXis (AMAX)-DOAS is a new technique for application from aircraft.
f) Direct sunlight observation of trace gases from balloon platforms allows the determination of trace gas profiles.

An extremely important, new application is satellite-borne DOAS, pioneered by the GOME and SCIA-MACHY instruments [19.29, 30] that allow observation of global stratospheric and tropospheric trace gas distributions (Fig. 19.11):

g) The most basic observation geometry is the nadir view. Here, sunlight backscattered from the Earth and its atmosphere is analyzed by DOAS to yield trace gas slant column densities. Ideally all light
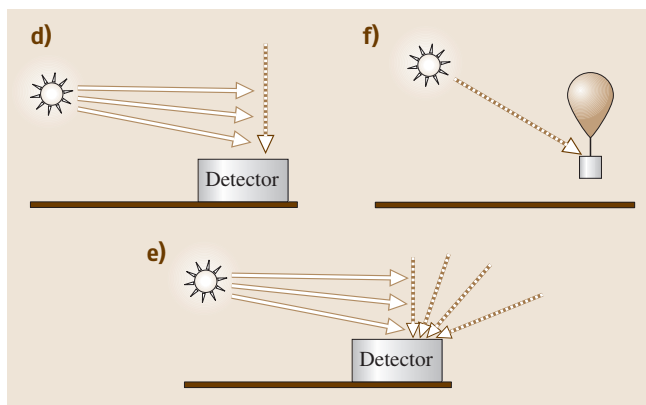
Fig. 19.10d–f The passive DOAS technique can be applied in several light path arrangements and observation modes using natural light sources such as sunlight or moonlight. The zenith scattered light (ZSL-DOAS) set-up (**d**) is most suited for the determination of stratospheric species, while the Multi-AXis (MAX-DOAS) arrangement (**e**) provides highly sensitive trace gas measurements in the atmospheric boundary layer. Direct sunlight observation of trace gases from balloon platforms (**f**) allows the determination of trace gas profiles in the atmosphere

recorded by the satellite spectrometer traversed the atmosphere twice.

h) Satellites also allow the observation of scattered sunlight in a limb-viewing geometry. This allows the determination of trace gas profiles (although generally only for the stratosphere).

i) Occultation (sunset, sunrise or starlight) measurements from satellites are an attractive possibility.

In addition it is now possible to determine the photon path-length distribution in clouds by ground-based observation of O_2 and O_4 bands. Here effectively DOAS is reversed: instead of the usual configuration where an unknown concentration is measured while the length of the light path is (at least approximately) known, the photon path-lengths are determined by observing the absorption due to an absorber with known concentration, such as oxygen (O_2) or oxygen dimers (O_4).

19.5.4 Atmospheric Aerosols

The atmospheric aerosol concentration is frequently monitored by light detection and ranging (LIDAR) instruments operated from the ground, aircrafts, or satellites [19.32]. In their most basic configuration they measure the ratio of total extinction due to Mie and

Fig. 19.11g–i Satellite-based DOAS has become an important technique for probing the atmospheric composition on a global scale. The most basic observation geometry is the nadir view (**g**), here sunlight backscattered from the Earth and its atmosphere is analyzed by D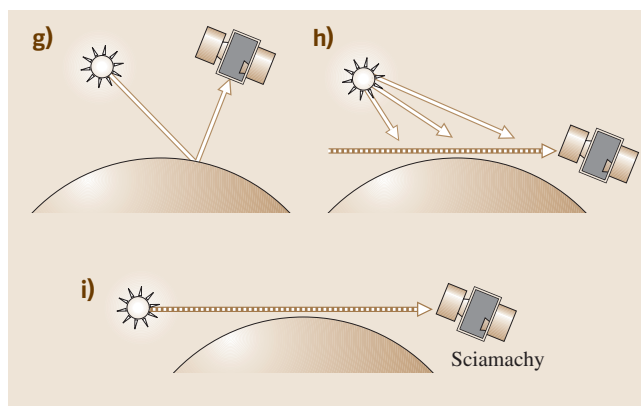OAS to yield trace gas slant-column densities. Ideally all light recorded by the satellite spectrometer traversed the atmosphere twice. Satellites also allow the observation of scattered sunlight in a limb-viewing geometry (**h**). This allows the determination of trace gas profiles (although generally only for the stratosphere). Occultation (sunset, sunrise or starlight) measurements (**i**) from satellite are another attractive possibility to determine trace gas vertical profiles

Table 19.3 Selection of species of atmospheric relevance measurable by DOAS and detection limits. Differential absorption cross-sections and corresponding detection limits (assuming 32 passes in a multi-reflection cell with a 8 m base path) for a series of species to be investigated by DOAS in the Valencia smog chamber. A dielectric mirror coating or DOAS measurements in the open atmosphere would allow longer light paths, resulting in correspondingly improved detection limits

Species	Wavelength of prominent band (nm)	Differential abs. cross section (σ_i') (10^{-20} cm²/molec.)	Detection limit $L = (40 - 8) \times 8\,\text{m} = 256\,\text{m}$ (ppt)
ClO	280	350	200
BrO	328	1040	80
IO	427	1700	50
SO$_2$	300	68	1000
NO$_2$	430	17	2700
HONO	352	41	2000
O$_3$	282	10	8000
Glyoxal[b]	ca. 470	≈ 10	≈ 8000
Benzene	253	200[a]	400
Toluene	267	200[a]	400
Phenol	275	3700[a]	20
Xylenes	260–272	≈ 100[a]	≈ 800
Benzaldehyde	285	500[a]	160

[a] data from Trost et al. 1997, R. Volkamer, personal communication 2000 [b] from [19.31]
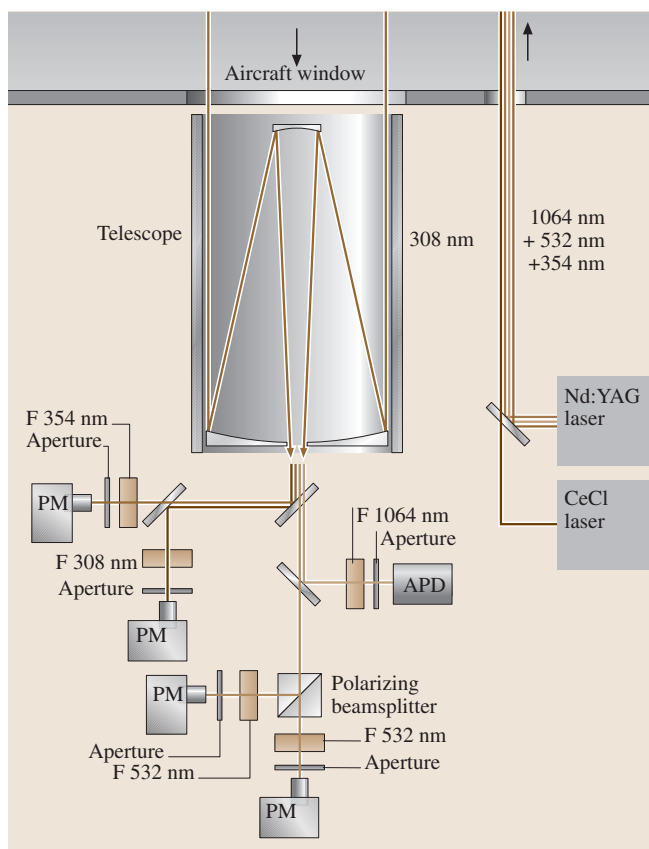
Fig. 19.12 Schematic setup of the DLR-Oberpfaffenhofen aircraft-borne LIDAR system (OLEX). APD: avalanche photo diode; PM: photomultiplier (courtesy G. Ehret/DLR Oberpfaffenhofen)

The Ozone Lidar EXperiment (OLEX) LIDAR is used as an aerosol and ozone LIDAR (Fig. 19.12). The system consists of two laser transmitters: 1) a Nd:YAG laser operating at a repetition rate of 10 Hz in the fundamental, second harmonic, and third harmonic with output energies of 200 mJ at 1064 nm, 120 mJ at 532 nm, and 180 mJ at 355 nm, and 2) a XeCl laser operating at 10 Hz, emitting 200 mJ at 308 nm. The receiver system is based on a 35 cm Cassegrain telescope with a field of view (FOV) of 1 mrad and a focal length of 500 cm. The system uses five detection channels: one channel for 1064 nm, two channels for 532 nm in two polarization planes, one channel for 355 nm, and one for 308 nm. The 308 and 355 nm channels are specifically dedicated to ozone profiling in the stratosphere, while the other wavelengths are used for aerosol and cloud monitoring. The acquisition electronics can acquire each single signature, with the lasers firing at a 50 Hz repetition rate, and the aerosol distributions measured by the system are available in real time. The total weight of the system is about 270 kg and the total power consumption above 1.6 kW.

In the present example, the OLEX LIDAR was assembled on board the DLR-Falcon aircraft in a down-looking mode that enabled aerosol backscattering measurements below the aircraft cruise altitude. On 24 September 1999, a flight was undertaken leading from Oberpfaffenhofen near Munich to the Adriatic Sea. The

Rayleigh scattering versus the calculated expectation of pure Rayleigh scattering for a set of absorbing and non-absorbing wavelengths.
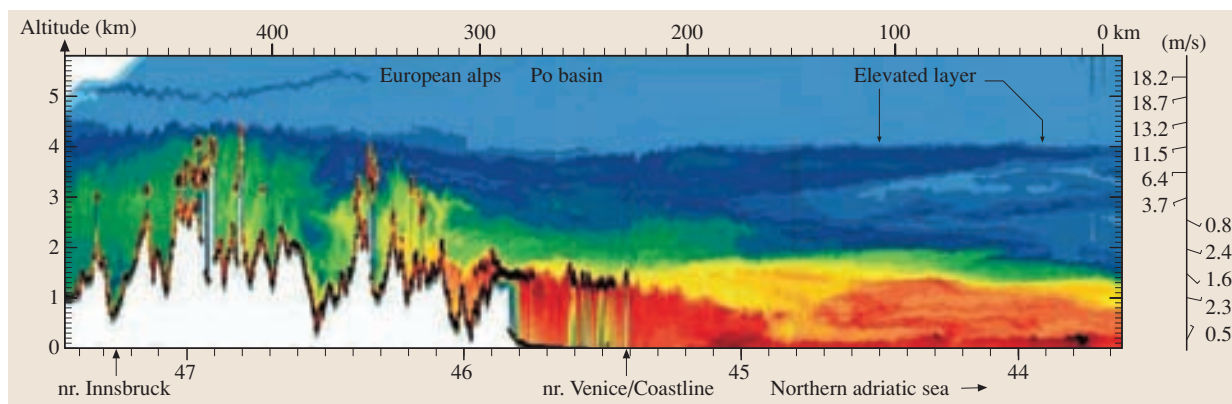

Fig. 19.13 Tropospheric aerosol distribution recorded by OLEX at $\lambda = 1024$ nm during a flight of the Falcon aircraft from Oberpfaffenhofen to the Adriatic Sea on 24 September 1999. The color codes qualitatively indicates the aerosol concentration with the large aerosol concentrations given in yellow and the small in blue color

main scientific objective was to investigate the spatial distribution of made-man aerosols emitted from traffic, industry and house burning into the lower troposphere.

The major detected features were inhomogeneously aerosol-loaded air masses located in the alpine mountain valleys and the fairly uniform planetary boundary layer (PBL) stretching over the whole alpine ridge (Fig. 19.13). Both aerosol layers nicely mark the vertical layering of a vertically layered lower troposphere typical for a high-pressure system at mid-latitudes in fall. Another interesting feature was the structure of the planetary boundary layer (PBL) located over the Adriatic Sea (≈ 2000 m above sea level), which overlaid a very thin marine boundary layer ($250-300$ m above sea level). This feature resulted from an advection of polluted PBL air masses originating from the North Italian Apennines and the Po Basin by synoptic westerly winds [19.33].

19.5.5 Determination of the Distribution of Solar Photon Path Lengths

A novel application of differential optical absorption spectroscopy (DOAS) is the measurements of path-length distributions of solar photons (photon PDF) transmitted to the ground [19.34–38]. The knowledge of a photon PDFs is of primary interest in the cloudy atmospheric radiative transfer, atmospheric absorption of solar radiation energy and thus for climate. The method relies on the analysis of highly resolved oxygen A-band ($762-775$ nm) spectra (Fig. 19.14) observed with a telescope with a small field of view ($1°$) in zenith-scattered sky light. It uses the fact that solar photons are randomly scattered by molecules, aerosols and cloud droplet during their atmospheric transport. Since a fraction of the solar photons become absorbed in the atmosphere, largely depending on the atmospheric opacity for a given wavelength, for each wavelength solar photons travel on different average, long distances in the atmosphere. Spectral intervals with a largely changing atmospheric opacity but known absorber concentration and spectroscopic constants, such as that given by the oxygen A-band, thus contain information on the photon PDFs. Recent studies have been showing that the atmospheric photon PDFs are highly correlating with the total amount of liquid water in the atmosphere, the spatial arrangement of clouds, cloud inhomogeneity and solar illumination [19.34–38]. For example, for thunder-
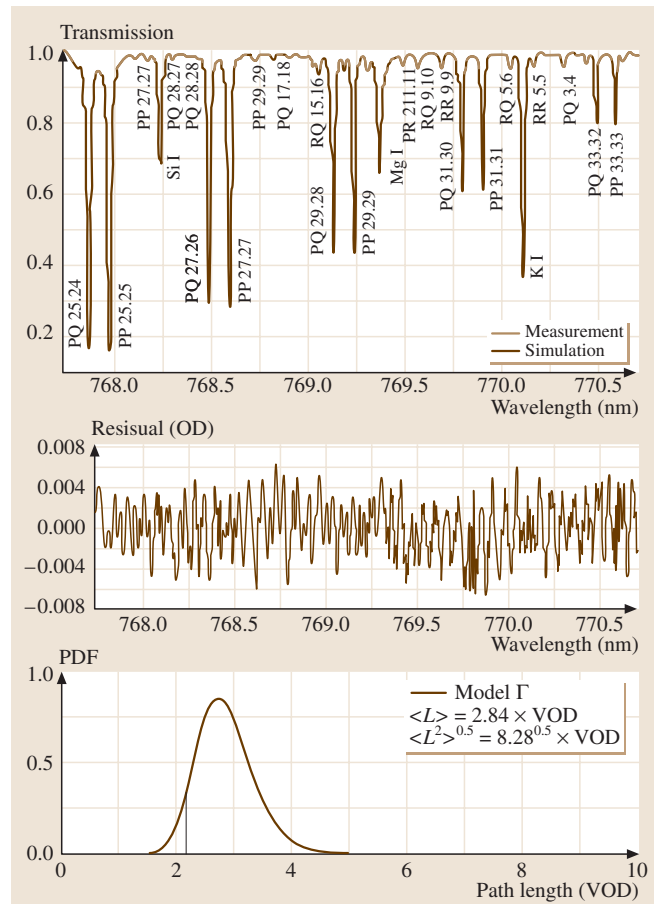
Fig. 19.14 Measured and modeled oxygen A-band spectrum (*upper panel*), inferred residual spectrum (*middle panel*) and inferred photon PDF for the observation between 12:32 and 12:33 UT over Cabauw/NL on 23 September 2001. The *black vertical line* indicates the optical path for the direct sunlight. Photon path lengths are given in units of vertical atmosphere (VOD) or air mass (AM)

storm Cb (cumulus nimbus) clouds, average photon path lengths of up to 100 km have been observed, while for Sc (stratus clouds) typically photon paths are $50-100\%$ larger than for the direct and slant path of the sun's rays. Moreover, it appears that even though the spatial distribution of cloud droplets is inhomogeneous with the moments of the density behaving like multi-fractals, photon PDFs tend to be mono-fractals, mostly due to the so-called radiative smoothing of optically thick clouds [19.39].

19.6 Optical Phenomena in the Atmosphere

Phenomena based on atmospheric optics can be observed nearly every day and everywhere. Examples are rainbows, halos, mirages, coronas, glories, the colors of the sky, sunsets and twilight phenomena, green flashes, noctilucent clouds, polar lights, and many more. All these different phenomena are due to interaction of light with matter present in the atmosphere (Fig. 19.15).

In the following, a brief survey of light scattering by molecules and particles with regard to optical phenomena in the atmosphere will be given. More details on light scattering by particles can be found in a number of monographs [19.40–43]. Several books have focussed on one or more optical phenomena (e.g. [19.44–54]). Some older original publications are available as a collection of articles [19.55] and the proceedings of the regular conferences on atmospheric optics have been published in special issues of the journals of the Optical Society of America [19.56–63], most of them recently put together on a CD-ROM [19.64]. Several videos and movies deal with selected phenomena [19.65–69], some articles focus on connections to the fine arts [19.70–73], a number of books focus on simple experiments as well as observations [19.74, 75] and a number of internet sites with a lot of material are also available, Table 19.4.
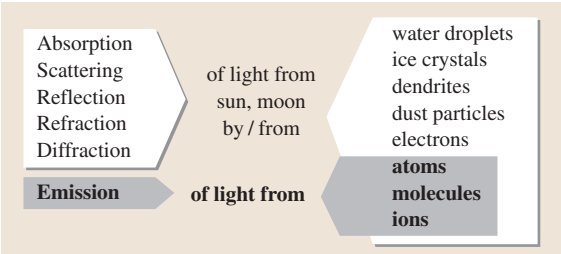
Fig. 19.15 Possible interaction processes of light with constituents of air

19.6.1 Characteristics of Light Scattering by Molecules and Particles

Nearly all optical phenomena in the atmosphere are due to light scattering – mostly sunlight and sometimes moonlight – with the constituents of air. In the following, a brief general survey of light scattering processes in the atmosphere will be given. Consequences for various optical phenomena of the atmosphere will be systematically discussed in the respective sections according to the constituents of the air that are responsible (Table 19.5).

Table 19.4 List of internet sites on atmospheric optics

1.	http://www.polarimage.fi (Images of many phenomena)
2.	http://www.atoptics.co.uk (Images and simulations)
3.	http://www.engl.paraselene.de (Images)
4.	http://www.philiplaven.com (Images and simulations)
5.	http://www.funet.fi/pub/astro/html/eng/obs/meteoptic/links.html (Finnish amateur observer site)
6.	http://www.ursa.fi/english.html (Finnish astronomical association)
7.	http://www.meteoros.de (German halo observer network)
8.	http://mintaka.sdsu.edu/GF/ (Green flashes)
9.	http://thunder.msfc.nasa.gov (Nasa lightning page)
10.	http://www.fma-research.com/ (Lightning, in particular sprites)
11.	http://www.sel.noaa.gov/ (Space weather)
12.	http://www.spaceweather.com/ (Space weather)
13.	http://sunearth.gsfc.nasa.gov/ (Nasa Sun Earth connection, outreach)
14.	http://www.mreclipse.com/ (Eclipses)
15.	http://www.geo.mtu.edu/weather/aurora/ (Auroras)
16.	http://www.exploratorium.edu/auroras/index.html (Auroras)
17.	http://www.amsmeteors.org/ (American meteor society)
18.	http://www.imo.net/ (International meteor organization)
19.	http://liftoff.msfc.nasa.gov/academy/space/solarsystem/meteors/Showers.html (Meteor showers, Nasa)

Table 19.5 Classification of optical phenomena of the atmosphere. Depending on the homogeneity of the air, different light interaction processes correspond to various phenomena, which are indicated by examples

1. Pure homogeneous air

- refraction $\Rightarrow$ mirages, shape changes of sun/moon at horizon Sect. 19.6.2
- scattering $\Rightarrow$ blue sky Sect. 19.6.3

2. Inhomogenous atmosphere: Air plus water droplets

- refraction and reflection $\Rightarrow$ rainbows Sect. 19.6.4
- forward scattering/diffraction $\Rightarrow$ coronas Sect. 19.6.5
- backward scattering/diffraction $\Rightarrow$ glories Sect. 19.6.5

3. Inhomogenous atmosphere: Air plus ice crystals

- refraction and reflection $\Rightarrow$ halos Sect. 19.6.6
- forward scattering/diffraction $\Rightarrow$ coronas Sect. 19.6.5

4. Inhomogenous atmosphere: Air plus aerosols

- absorption, scattering $\Rightarrow$ sky colors Sect. 19.6.7
- absorption, scattering $\Rightarrow$ visibility Sect. 19.6.8
- forward scattering/diffraction $\Rightarrow$ coronas Sect. 19.6.5

5. Ionized air

- ionization/excitation by solar wind, emission $\Rightarrow$ auroras Sect. 19.6.9
- ionization/excitation by discharges, emission $\Rightarrow$ lightning Sect. 19.6.9

Molecular Scattering

For pure air, scatterers are mostly N_2 and O_2 molecules, the greenhouse gases CO_2 and H_2O as well as some traces of other gases such as Ar [19.76]. These scatterers are all much smaller than the wavelength of visible light and one speaks of a molecular atmosphere [19.77]. The vertical distribution of the gaseous components of air follows the barometric formula with a scaling height of about 8 km. The scattering of sunlight from the bound electrons of atoms/molecules is usually called Rayleigh scattering [19.1, 78, 79]. (For historical notes on the problem of the blue sky, see [19.80].)

Scattering from Particles

Normal air usually also contains a variety of different particles, the most predominant being water droplets, ice crystals and snow flakes (dendrites). The size of the water droplets ranges from several micrometers (cloud droplets) to well above 1 mm (raindrops); ice crystals are very often of hexagonal symmetry with sizes on the order of $10-100\,\mu m$.

In addition, the atmosphere also contains other liquid and solid particles called aerosols [19.20, 76, 81, 82]. These include many types of particles from dust, oil droplets from forest fires, volcanic ashes as well as anthropogenic droplets/particles with an enormous variety in composition. Typical aerosol particles have size distributions in the range $0.1-10\,\mu m$ with an average around $1\,\mu m$ (e.g. [19.83]). The vertical distribution of the particle components of air may also be described by some kind of exponential formula [19.77], however, the scaling height of $1-2$ km is much smaller than that for molecules.

The scattering of light from particles in these size ranges differs dramatically from molecular scattering, since the particle size is comparable to or larger than the wavelength of the light. Since atoms/molecules within particles are very close to each other, they are excited coherently, i. e. the total scattering from all molecules within a particle is quite different from the sum of the scattering of all individual molecules within the particle. In 1908, *G. Mie* gave the solution of classical electrodynamics for the simplest case, referring to spherical shapes of the particles [19.10]. Henceforth, this type of light scattering from particles is mostly known as Mie scattering. This name is sometimes also used for extensions to nonspherical particle shapes. For nonabsorbing particles, which are small compared to the wavelength, the Mie scattering gives the same results as Rayleigh scattering. In the general case, however, it shows pro-

nounced differences regarding wavelength dependence, angular dependence, degree of polarization of the scattered radiation as well as scattering cross section per molecule [19.40–42, 77].

Comparison of Rayleigh and Mie Scattering

Wavelength Dependence. Figure 19.16 gives a schematic example of the scattering of light by water molecules as well as water droplets of, say, 10 μm. Whereas molecules or very small particles scatter light mostly according to the inverse fourth power of wave-
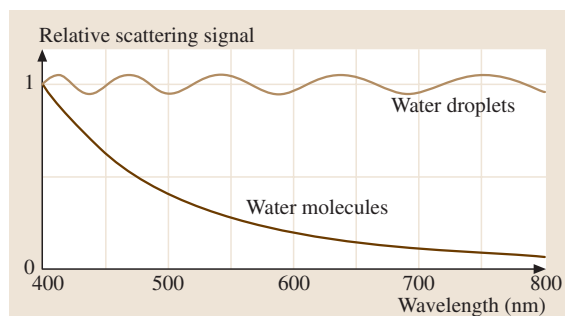
Fig. 19.16 Schematic wavelength dependence for light scattering from water molecules and water droplets of, e.g., 10 μm size

Fig. 19.17 Schematic overview of the angular dependence of light scattering from molecules and very small particles (Rayleigh scattering) to larger particles (Mie scattering)
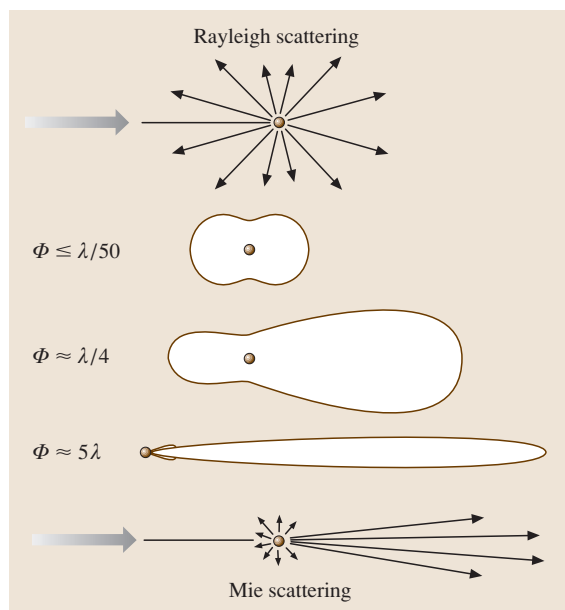
length, scattering from water droplets is essentially independent of wavelength.

Angular Dependence. Figure 19.17 gives a schematic overview of how the angular dependence of scattering changes with particle size. Molecules scatter unpolarized light nearly isotropically (see also Fig. 19.1) whereas large particles scatter rather asymmetrically in the forward direction. For a given particle size, the scattering also depends on wavelength.

Degree of Polarization. For Rayleigh scattering, and assuming perfectly spherical air molecules, light scattered at an angle of 90° would be perfectly polarized [19.84]. However, air molecules already show an anisotropy, reducing the polarization to only about 94% [19.77, 79]. For larger particles, the degree of polarization varies considerably as a function of scattering angle for fixed size. These patterns, however, strongly depend on size [19.40, 41, 77]. In addition, the degree of polarization at a fixed angle varies as a function of wavelength.

Scattering Cross Section per Molecule:. The enormous differences between incoherent and coherent scattering become apparent when comparing light scattering from isolated molecules to those of the same molecules within a particle, e.g. water molecules within a water droplet or a raindrop [19.77]. For example, the scattering per molecule that belongs to a cloud droplet of 1 μm is about 10^9 times larger than scattering by an isolated water molecule and still a factor of about 100 larger than a molecules in a 1 mm raindrop.

Single and Multiple Scattering, Optical Mean Free Path and Air Mass

Light from the sun (or moon) has to traverse the atmosphere before reaching the eye of an earthbound observer. It is attenuated by scattering and absorption, depending on the number of scatterers present in the line of sight. If absorption can be neglected, one may use the scattering coefficient

$$\beta_S = N\sigma , \tag{19.35}$$

where N is the number of scatterers per unit volume and σ is the extinction cross section, $1/\beta_S$ defines the scattering mean free path, i. e. the average distance a photon has to travel before being scattered. (If absorption is included, an additional absorption coefficient β_A is introduced and β_S will be replaced by $\beta = \beta_S + \beta_A$.) Using β_S, one may define the optical thickness τ between two

points A and B of the atmosphere as

$$\tau = \int_A^B \beta_S(x)\,dx \,. \tag{19.36}$$

The optical thickness is a measure of the physical thickness in units of the scattering mean free path. For light along a radial path, i.e. coming from the zenith, the amount of air to be traversed is least and one refers to the normal optical thickness, which is also called the optical depth. For a pure molecular atmosphere, this is depicted in Fig. 19.18. In the visible spectral range, its values are small compared with unity, hence, a photon is unlikely to be scattered more than once, i.e. single scattering predominates.

The amount of air to be traversed by light, the so called air mass, depends on the sun's elevation. Air mass (AM) is defined to be unity for the light source in the zenith. It increases for smaller sun elevation angles. As a matter of fact, it is the optical thickness, relative to its zenith value. The exact value depends on the surface pressure. At 5° elevation (85° zenith angle) its value is about 10 and it ultimately reaches a value of about 40 at grazing incidence [19.51, 77, 85, 86], i.e. for the case of sunrise or sunset. In this case, the light must pass about 40 times the amount of air compared to the case of the zenith.

Combining the air mass with the normal optical thickness gives the optical thickness for arbitrary sun elevation. Since AM reaches large values, optical thicknesses may become large compared with unity, i.e. multiple scattering events become likely for low sun elevations.

19.6.2 Mirages

Mirages are due to the propagation of light waves in air that has gradients in the index of refraction [19.44–48, 51]. In general, light which is propagating in clear air (no particles) is partly scattered according to Rayleigh scattering, while the rest propagates undisturbed in the forward direction. The scattered light consists of sideways scattering and forward scattering, the latter being in phase with the incident light. As a consequence, light in clear air is slightly weakened by sideways scattering, the forward-propagating light being the superposition of the incident light and the forward-scattered light. The weakening due to sideways scattering will be discussed below (blue sky). Here, the phenomena associated with the forward-propagating light will be
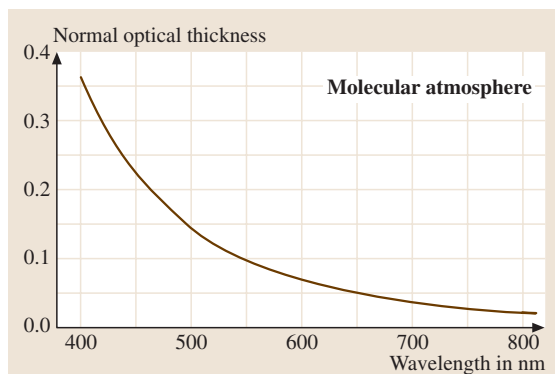
Fig. 19.18 Normal optical thickness of a purely molecular atmosphere (data from [19.3])

discussed. Scattering effects by particles are neglected here.

In homogeneous media, the forward propagation of light is expressed in terms of the refractive index n (for tables of n [19.3]). n depends on temperature T (in K), pressure p (in mbar) and humidity. Equation (19.37) [19.87] gives an approximation for n of dry air

$$n = 1 + \frac{77.6 p}{T} \times 10^{-6} \,. \tag{19.37}$$

For example, $T = 300\,\text{K}$ and $p = 1030\,\text{mbar}$ yields $n \approx 1.000266$. Increasing the air temperature by 40 K (e.g., air directly above the ground which is heated by the sun) gives $n \approx 1.000235$ (for humid air, the numbers only change slightly). These small changes of $\Delta n \approx 3 \times 10^{-5}$ are responsible for all kinds of mirages.

The most simple mirage effect is known from astronomy: if an observer looks at an object in the sky at a certain altitude, the actual position of the object is lower in the sky. This is due to the refraction of light upon propagation in the atmosphere with a gradient in n giving rise to curved light paths.

At the zenith, the deviation is zero, at 45° zenith distance it amounts to 1′ (1 minute of an arc) increasing to more than 38′ at an angle of 90°. This has to be compared with the angular size of the sun or moon, which is about 30′, i.e. half a degree. Since the refraction is only about 28′ at a zenith distance of 89.5°, the sun or the moon in an otherwise undisturbed atmosphere (no inversion layers) will thus be flattened [19.47], see also [19.88–92].

Mirages are images of objects which may be seen in addition to the real objects. They can be seen whenever there are temperature differences in the atmosphere,
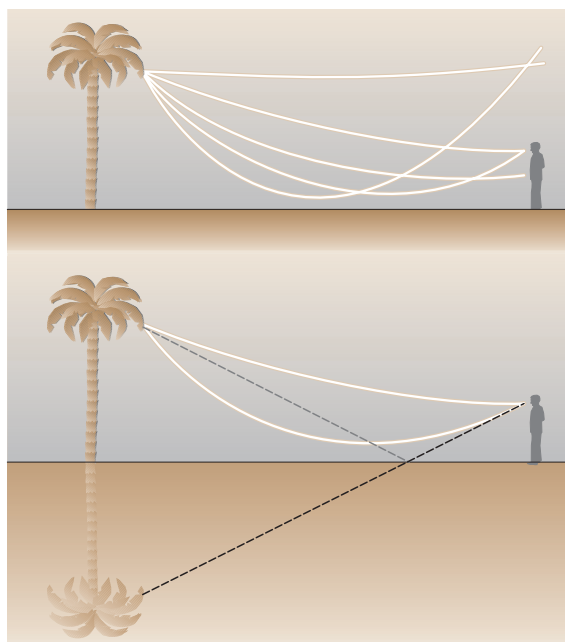
Fig. 19.19 Inferior mirage: a palm tree scatters sunlight in all directions. The atmosphere is heated close to the ground. Therefore the index of refraction is smaller there, giving rise to curved light paths. Direct and refracted light can enter the eye of an observer, which is interpreted as an object on top of an inverted image (after [19.48])

which give rise to unusual gradients in the index of refraction. Similarly to astronomical refraction, gradients in n give rise to curved light paths. If warm air is above the ground, n is smaller close to the ground than above it. This leads to inferior mirages like the well-known wet streets on hot summer days. The formation of inferior mirages is illustrated in Fig. 19.19. A prominent feature of a mirage is the so-called vanishing line of the object [19.48]. Light below certain object points has no chance whatsoever to reach the eye of the observer, i. e. parts of the object cannot be seen, irrespective of the direction into which the light is scattered.

In the case of an inversion layer in the atmosphere, the air at a given height is warmer than below, which may give rise to superior mirages. Similarly to inferior mirages, the propagation of light with curved paths in this case can give rise to multiple images on top of the object. In nature, combinations of inferior and superior mirages may occur. Also, heated vertical walls may result in lateral mirages.

The angular size of mirages is usually about 0.5–1.0°. For observations, binoculars and cameras with

telephoto lenses are used. The mirages are often distorted and flicker due to local density fluctuations in the air.

Theoretical progress in understanding mirages came with the computer. The propagation of light rays in a given atmosphere, defined by the vertically varying index of refraction $n(z)$, is computed theoretically using ray-tracing methods. The various methods [19.93–96] differ by their choice of geometry and $n(z)$. Such simulations prove very helpful in understanding the general characteristics of mirages, like e.g. so-called mock mirages [19.97, 98].

Recent research has explained many unusual mirage phenomena quantitatively, including long-range mirages like the Novaya–Zemlya effect from atmospheric ducting [19.99–102] and small-scale movements seen within superior mirages when atmospheric gravity (buoyancy) waves are present [19.103, 104].

Superior mirages seen over large distances (70–100 km) can result from fairly complex atmospheric temperature profiles [19.95]. Also, the origin of double inferior mirages as well as unusual horizontal stripes in inferior mirages has been analyzed theoretically [19.96]. Very recently, focus had been on very precise measurements and comparison to modeled astronomical refraction of the setting sun [19.105, 106] and the occurrence of very bright superior mirages [19.107].

In addition to analysis of observations and theoretical models, inferior mirages and superior mirages with multiple images may also be studied quantitatively or as demonstration experiments in the laboratory [19.65, 108–112].

19.6.3 Clear Sky: Blue Color and Polarization

Light scattering in pure gases is due to the electrons in atoms and molecules. As a result, the scattered light intensity varies approximately as $1/\lambda^4$ (Fig. 19.16), i. e., red light is scattered much less than blue light [19.1, 78, 79]. When looking at the daylight sky illuminated by the sun one mostly sees scattered light and, hence, a blue sky (In Sect. 19.6, the qualitative term intensity which is often not properly defined (see [19.113]), does usually mean either radiance, given in W/m^2 sr, or spectrally resolved radiance in W/m^2 sr nm).

The scattered light is strongly polarized at a scattering angle of 90° [19.84]. Concerning the whole sky, the polarization varies and also has neutral points, named after Arago and Babinet [19.44, 46, 51]. In reality, even if very clean air is used, the maximum degree

of polarization is about 94%, see Sect. 19.6.1. The atmosphere usually also contains an appreciable number of particles, which show Mie scattering with different angular polarization dependencies. In addition, there may be contributions of multiply scattered light as well as backscattering from the surface of the Earth. Overall, the degree of polarization typically reaches values around 80%. Obviously, this depends on the concentration of particles and is thus related to the transmission of the atmosphere [19.114]. More details on scattering effects and recent research will be given in Sect. 19.6.7.

19.6.4 Rainbows

Rainbows are due to scattering of sunlight from raindrops in the atmosphere [19.43–48, 51]. The drops are in the size range between $10\,\mu m$ (white fogbow/cloud bow) and several millimeters. One usually assumes spherical droplets, however, drop shapes may vary depending on size [19.115, 116] or they may even oscillate [19.117]. Drop formation and size distributions have been extensively studied [19.118]. The effect of nonsphericity on rainbow phenomena is discussed, e.g., in [19.119, 120].

The observed bows are mostly due to single scattering events. Hence, the complex problem of light scattering from millions of raindrops in a rain shower can be reduced to the scattering of sunlight from a single raindrop. Since raindrops are large compared to the wavelength of light, geometrical optics already gives a rough description. Figure 19.20 depicts a single raindrop and parallel light rays from the sun.

The rays are characterized by their impact parameter b. Each ray is reflected and refracted upon hitting an interface between air and water. For clarity, only the light paths that give rise to the primary rainbow are sketched. They are defined by refraction into the droplet, internal reflection and refraction back into the air. Similarly higher-order rainbows may be constructed by allowing for multiple internal reflections. The central ray (1) is not deflected by the refractions and exits at a scattering angle of 180° with respect to the incident ray. Ray number (2) suffers a scattering angle of about 170° and so on. For increasing impact parameter the scattering angle δ decreases until a minimum is reached at an impact parameter of about $0.86\,R$ (ray 7). The flatness of this shallow minimum (Fig. 19.20) at an angle of about 138° is responsible for the fact that much more light is scattered into this direction – geometrically along the surface of a cone – than in others, since many incoming light rays of slightly differing impact parameters will emerge in the same output di-
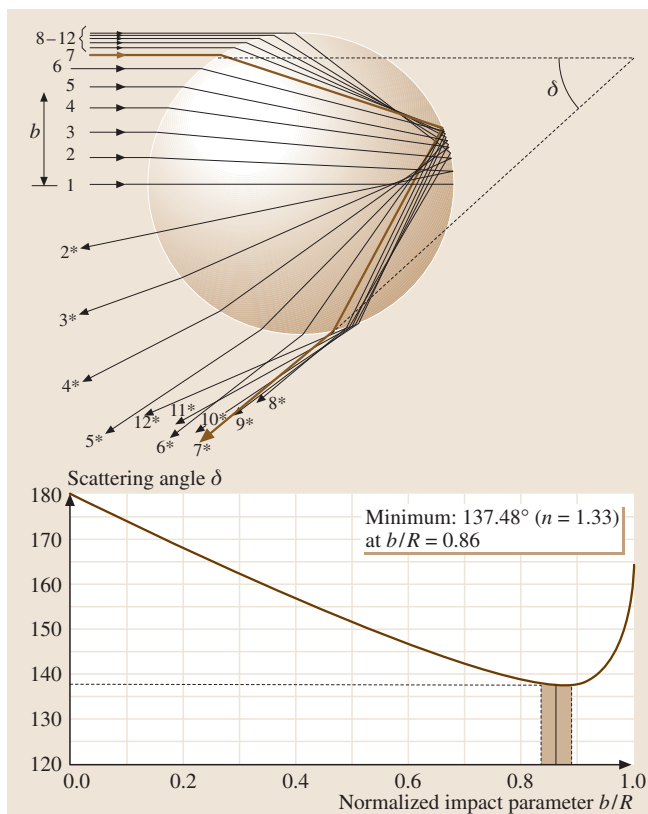
Fig. 19.20 Simple explanation of a rainbow from a single raindrop in terms of geometrical optics. Parallel light rays, characterized by the impact parameter b, are scattered due to refraction, internal reflection and refraction (for clarity other light paths are omitted). The scattering angle δ as a function of b exhibits a shallow minimum, i.e. many incoming light rays with different values of b will be scattered in the same direction

rection. As a consequence, an observer who is looking at a cloud of raindrops that is illuminated from the back by sunlight, will observe a bow of angular size 42° (Fig. 19.21).

The rainbow angle, i.e. the minimum of δ in the plot of Fig. 19.20, can be easily calculated (e.g. [19.47, 121]) with geometrical optics by finding the minimum of the scattering angle $\delta(\alpha_{inc})$ with respect to the angle of incidence α_{inc} of the light rays onto the droplet. Assuming $n_{air} \approx 1$ one finds for the primary bow

$$\delta(\alpha_{inc}) = 2\alpha_{inc} - 4\alpha_{refr} + \pi\,, \quad \text{with}$$

$$\cos\alpha_{inc} = \sqrt{\frac{n^2 - 1}{3}}\,. \tag{19.38}$$

Part D | 19.6
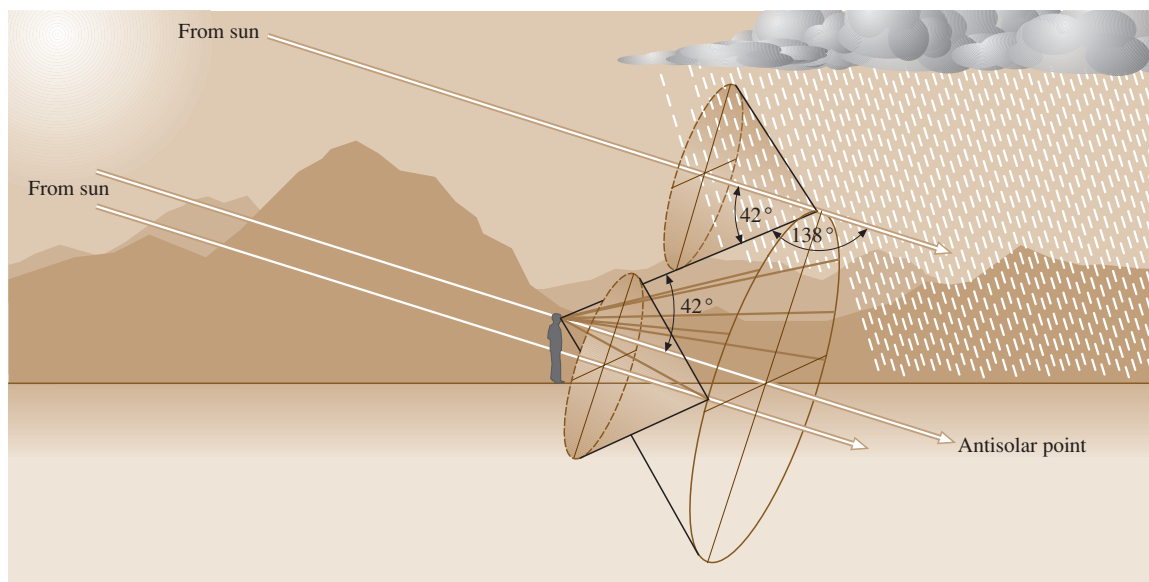
Fig. 19.21 Observation of a rainbow. Each raindrop scatters light preferably in a cone of the rainbow angle. Hence, an observer will see more light when looking in the direction of the surface of a cone that is centered in a droplet. The whole rainbow is due to millions of drops, the effect of which is an observable bright feature, geometrically on the surface of another cone centered in the eye of the observer and making an angle of 42° with regard to the antisolar point (after [19.48]). Its surface touches the surfaces of the scattered light cones of each individual droplet

Here α_{refr} denotes the angle of the refracted ray within the raindrop and n is the index of refraction of water. For $n = 1.33$, Snell's law gives a scattering angle of $\delta(\alpha_{\mathrm{inc}}) = 137.5°$. Due to dispersion ($n_{650\,\mathrm{nm}} = 1.331$, $n_{400\,\mathrm{nm}} = 1.343$) the rainbow angles depend on wavelength. Taking into account the finite size of the sun of about 0.5° one finds an angular width of about 2.2° for the primary bow. The analysis is easily extended to higher-order rainbows [19.47], most of which may, however, only be observed in the laboratory [19.110, 122–125].

Several rainbow features can only be explained by wave optics. Light from the rainbow is appreciably polarized perpendicular to the plane of incidence, since the angle of incidence for the internal reflection is close to the Brewster angle [19.126]. Also, careful measurements showed that the light intensity shows an interference pattern, named after Airy [19.50, 127, 128], which differs markedly from the prediction of geometrical optics (Fig. 19.22).

Until the beginning of the 20th century, wave optics features were computed using Airy's theory, which gives reasonable results for droplet sizes down to 10 µm; for smaller sizes, it fails. Improvements came with Mie theory [19.10, 40, 41], however, its numerical solutions in terms of scattering efficiencies as a function of angle for size distributions of the droplets and finite angular size of the solar disk had to wait for the development of computers. Similarly, Debye developed
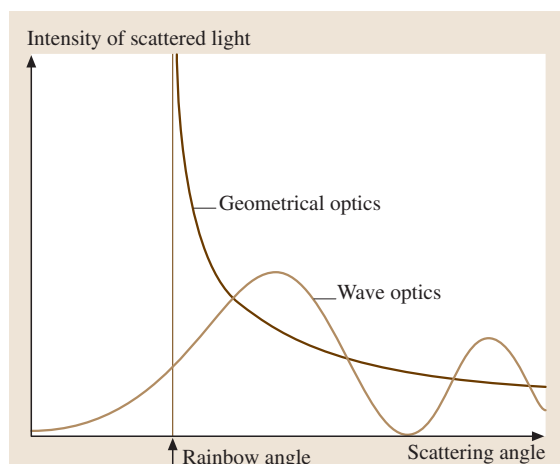
Fig. 19.22 Differences between the theories of Descartes and Airy for the scattered light intensity of raindrops

a tool of how to decompose the partial wave amplitudes for scattering of a plane wave into individual contributions of certain types. This later led to the complex angular-momentum theory [19.129]. Application of the mathematics of catastrophe theory to light scattering showed that the rainbow is a manifestation of the so-called fold caustic [19.130].

Here, results of the full electrodynamic treatment, i. e. Mie theory, are presented [19.40, 41, 131–133]. Figure 19.23 depicts results for monochromatic blue light of $\lambda = 450$ nm, scattered by a lognormal distribution of water droplets with mean radii ranging from 2 μm to 200 μm. The full width at half maximum of the size distribution is 10% of the mean radius.

Obviously, large droplets show Airy rings at the rainbow angles. For other wavelengths, these curves would be slightly shifted due to dispersion. The overlapping of the interference rings for all wavelengths leads to so-called supernumerary arcs (e.g. [19.134, 135]). Decreasing the droplet size leads to a broadening of the rainbows due to diffraction. In this case, the overlapping of all wavelengths leads to a white rainbow, also called a fog bow. If the size becomes too small, no rainbows are observable. The other features in Fig. 19.23 will be discussed in Sect. 19.6.5.

There are many other interesting features of rainbows. For example the first-order rainbow often visually appears brighter at the base of the bow than at the top of the bow. This is due to the fact that, in a rain shower, raindrops are distorted in shape to oblate spheroids. Light reaching an observer from the base of a rainbow traverses a water droplet in the horizontal plane where the droplet cross section is circular. In contrast, light from the top of the rainbow traverses the water droplet in the vertical plane where the droplet cross section is elliptical. Since the scattered light intensity due to the internal reflection is less in the elliptical cross section than that in the circular cross section the base of the rainbow is brighter than the top of the bow (the longer optical path from the top may also lead to increased extinction).

Similar explanations [19.136] are possible for other features such as, e.g., that the supernumeraries of the first-order rainbow often appear most vividly at the top of the bow or that supernumeraries of the second-order rainbow are almost never seen. Also, the effects of the electric fields [19.137] and acoustic forces accompanying thunderstorms can have observable consequences on rainbows [19.117]. Visibility and general brightness of rainbows depend on multiply scattered and absorbed
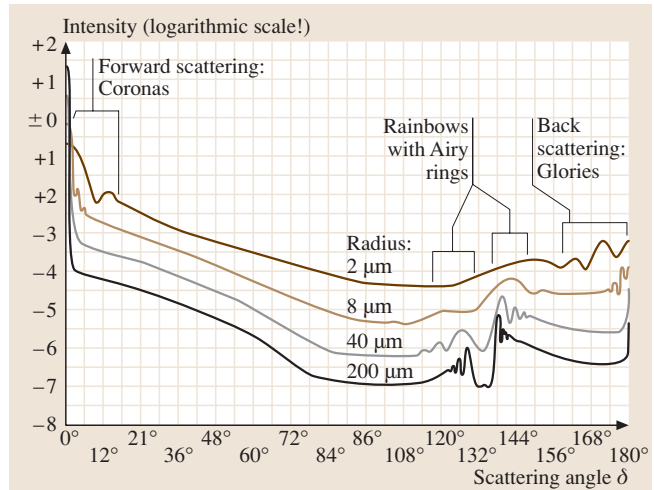
Fig. 19.23 Angular distribution of blue light scattered by water droplets with mean radii ranging from 2 μm and 8 μm (fog and cloud droplets) to 200 μm (small raindrops) (computation by E. Tränkle)

light [19.138, 139]. Even infrared rainbows have been detected [19.140].

In addition to analysis of observations and theoretical models, rainbow phenomena may also be studied in the laboratory either for quantitative comparison to theory or just as demonstration experiments using either single droplets or cylinders of water or other materials [19.109, 110, 122–124, 136, 141, 142].

Present investigations of rainbow phenomena deal, e.g., with experiments on higher-order rainbows from acoustically levitated water drops [19.143] or cylinders [19.144, 145] and total internal reflection rainbows [19.146] as well as new simulations of rainbows and fogbows [19.147, 148].

19.6.5 Coronas, Iridescence and Glories

The forward and backward scattering of small water droplets can also give rise to very distinct features [19.43, 44, 47, 48, 51]. First, colored concentric rings, called coronas, around the sun or the moon with angular distances up to, e.g., 15° may be observed, when looking through thin clouds. The middle whitish part around the light source is often called an aureole. If, second, colorful clouds are observed at larger distances from the sun (up to 45°), one usually speaks of cloud iridescence. Third, backscattering that leads to colorful concentric rings at angles close to 180° with respect to the light source are called glories. Figure 19.24 gives an
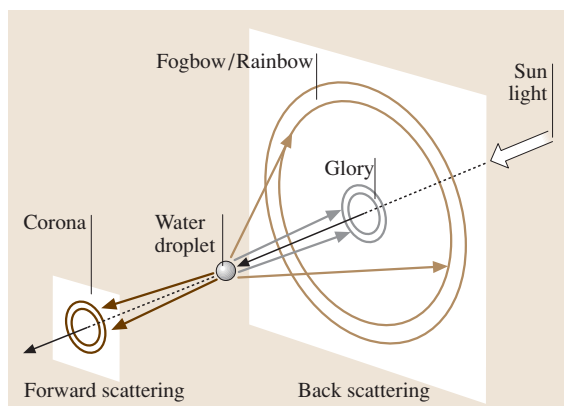
Fig. 19.24 Overview of geometries of light-scattering phenomena from a water droplet

overview of the light-scattering geometries of rainbows, coronas and glories due to water droplets.

Coronas

In its most spectacular form, coronas can be observed as a concentric series of three or four brilliantly colored rings around the sun or moon. In its simplest form, the corona is just represented by the aureole, which is a white disk near the sun or moon bordered by a bluish ring and terminated by a reddish-brown band.

Coronas are easily explained using Mie theory [19.149, 150]. Coronas occur as strong forward-scattering phenomena (Fig. 19.23) for very small nearly monodisperse sizes of typically about 10 μm. More simply, coronas are treated as diffraction phenomena by water droplets. The first minimum for light of wavelength λ diffracted by a circular aperture of diameter $2R = D$ is given by

$$D \sin \phi = 1.22\lambda . \tag{19.39}$$

For droplets of nearly uniform size, the diffraction angles ϕ obviously depend on wavelength, giving rise to rather pure perceived colors of the coronas. In this case, the average droplet size may be estimated from the angular size of the rings from (19.39). To obtain the approximate angle for the red band of the solar corona, it is customary to use $\lambda = 570$ nm in (19.39) since the positions of the red bands are believed to correspond to the minima for green light [19.151]. (Alternatively to 570 nm, 490 nm has been proposed [19.152].) For example, $2R = 10$ μm gives $\phi \approx 4°$. (Note that there will be deviations between the correct Mie theory and diffraction theory for droplets with sizes of 10 μm and below.) A much better way to judge droplet sizes is to fit the col-

ored rings of computer simulations to those of photos of natural observations [19.150].

An aureole may be produced by relatively large particles that tightly compress the rings, or by the presence of a broad particle size distribution that causes the colored rings to overlap.

Simple diffraction theory has problems for drops with sizes only slightly greater than the incident wavelength. In this case, Mie theory must be applied, since the amplitudes of the diffracted and transmitted light are comparable in the forward-scattering direction, leading to interference between the two components that can significantly alter the scattering pattern.

The nature of the cloud particles that cause coronas has been the subject of controversy [19.152, 153]. Observations of some coronas due to very high clouds suggested that not only supercooled spherical cloud droplets, but also ice crystals may be responsible for coronas. However, ice crystals can assume a variety of shapes and orientations that should not give very pure coronal colors. The issue was settled by experiments which simultaneously used polarization LIDAR data as well as photographic evidence of coronas to demonstrate that cirrus clouds composed of hexagonal ice crystals with particle sizes ranging from 12 to 30 μm (which is unusually small for most cirrus clouds) can generate multiple-ringed colored coronas [19.152]. Later the study also included aircraft probes of the particles [19.153]. In one case a weak corona and a halo display (see below) of the hexagonal crystals were observed simultaneously within the same cloud. This is possible, since laboratory experiments indicate a lower limit of about 20 μm for the sizes of ice crystals that can produce halo effects.

Some while ago, it was also noted that coronas need not be spherical. Elliptical coronas have been reported at special times in early summer. They were explained as diffraction phenomena from nonspherical birch and pine pollen grains [19.154–156]. Also, split coronas due to local variations of droplet size or changes between water and ice have been observed [19.157]. Recently, new simulations have been reported [19.158]. Special coronas, called Bishop's rings, can be produced by volcanic ashes, as has been reported after the explosion of Krakatau in 1883.

Iridescence

Cloud iridescence is a brilliant display, which occurs quite often when appropriate thin clouds are close to the sun or moon or if edges of thick clouds happen to

have rather monodisperse droplets. Iridescence is also observed, though more rarely, at much larger angular separation from the sun of up to 45° and it may be easily observed and analyzed within contrails [19.151]. If interpreted using diffraction, like coronas, the drop sizes $2R$ are in the range $2-4\,\mu m$. These sizes are indeed quite rare, though possible near the edges of growing or evaporating clouds.

Whereas, coronas are generally observed at smaller angles for mostly monodisperse droplet populations with sizes of about $10\,\mu m$, iridescence usually occurs at larger angles and requires cloud droplet sizes on the order of a few microns in diameter with broad size distributions. These conditions are often found in the vicinity of the visible cloud margin where there is also a sharp gradient of the drop sizes. Thus, coronas and iridescence appear to require quite different cloud microphysical conditions to be present, and should also be most frequently observed in different angular regions [19.151]. Recent studies deal with coronas and iridescence in mountain wave clouds [19.157] as well as rare iridescence cases in cirrus clouds [19.159, 160].

Glories

The colored rings of glories, sometimes also called spectre of the Brocken are observed in a backscattering geometry, if sunlight illuminates fog or clouds with very small water droplets. Nowadays, observations can be performed easily when flying in airplanes and observing the shadow of the plane on nearby clouds.

Early interpretations could not use Mie theory (since computers were not available), but tried to understand the phenomenon in simpler terms. The assumption of diffraction of reflected light by the droplets (diffraction from circular apertures) did not work, since intensities and angular distances of the pattern are different. However, diffraction from circular rings could explain the phenomenon [19.40, 161]. For this to happen, glories must be due to light entering the raindrops at grazing incidence (this interpretation was later supported by Mie theory [19.162]). Then, the scattered light is more or less exiting at the opposite side of a droplet, i.e. at scattering angles of 180°. In terms of geometrical optics, this is not possible, however, wave theory allows for surface waves at the boundary. In the backward direction, all contributions interfere constructively to produce the glory. These model assumptions were supported by experiments with microscopic water droplets supported by submicroscopic spider webs [19.163]. Later on, this model was further developed very successfully [19.129]. Nowadays, glories are explained by using Mie theory.

Glories are present in Fig. 19.23 as oscillatory structures in the angular range from about 160 to 180° for droplets of 4 and $16\,\mu m$ size. The more uniform the droplet size, the more rings may be observed.

Knowing from coronas that colorful rings may also be produced by fairly monodisperse assemblies of ice crystals and even tree pollen, one may ask whether the glories that are often observed from airplane windows may also be due to ice crystals in high-altitude cirrus clouds.

From the above interpretation of Mie theory, the glory is due to circumferential, i.e., surface-wave ray paths which are unique to spheres. Glories are, hence, produced by spherical scatterers. Based on photographic evidence, it was therefore investigated [19.164] whether glories may be also due to spherical or near-spherical ice crystals? In conclusion it was found that ice grows in amorphous and presumably spherical shapes only at unlikely frigid temperatures. Recent studies have, however, suggested that small near-spherical ice particles (diameters ranging from 9 to $15\,\mu m$) can sometimes, though very rarely, occur near the tops or along the margins of some ice clouds, and these may give rise to observable glories. Very recently, new simulations for glories were reported [19.147, 165, 166].

19.6.6 Halos

Halos are caused by the refraction and/or reflection of sunlight by ice crystals in the atmosphere [19.43–48, 51, 52, 66, 167]. They can already be understood in terms of geometrical optics. Ice crystals that cause good halo displays are usually hexagonal plate or column crystals with sizes in the range of $20-100\,\mu m$ [19.168]. Such crystals form very often, depending on the temperature and the amount of water vapor in the air [19.169]. Good documentation with micrographs can be found in the literature [19.52, 170].

A great number of different halos may be observed in nature and in the laboratory since there is an enormous variety of possible types of ray paths through the crystals and crystals may have different orientations in the air.

The most simple halos are parhelia, also called sun dogs, which are often observed in cirrus clouds (and sometimes in contrails [19.171]). They are due to oriented plate crystals, i.e. crystals falling with their principal axes vertical. This orientation mode is often possible and is, e.g., similar to movements of leaves (or sky divers), which maximize their air resistance as they fall [19.118]. If light rays from the sun enter a prism face
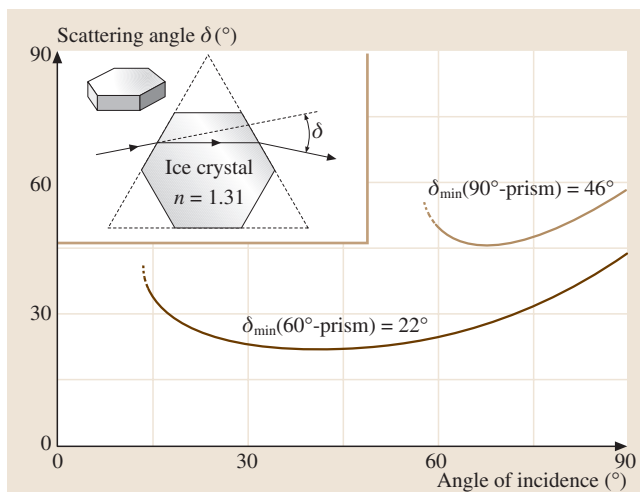
Fig. 19.25 Ray paths within hexagonal ice crystals ($n = 1.31$) show an angle of minimum deviation of 22°. For clarity, other light paths are omitted

of a crystal and exit an alternate prism face, the situation corresponds to refraction from a 60° prism. The scattering angle as a function of angle of incidence shows a flat minimum (Fig. 19.25) that is at a scattering angle of 22° for ice crystals with $n = 1.31$. Similarly to the explanation of the rainbow, more light is deflected in this direction. Therefore an observer looking at the sun or the moon through a thin cirrus cloud will see more light at an angular distance of 22° from the light source. For randomly oriented crystals, the resulting display will be
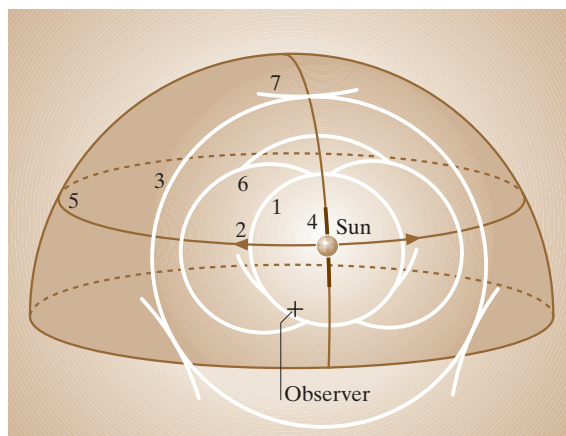
Fig. 19.26 A schematic survey of some halos which may be observed (1: 22° halo, 2: parhelia, 3: 46° halo, 4: sun pillar, 5: parhelic circle, 6: circumscribed halo, 7: circumzenithal arc). These displays all depend on sun elevation

a circular halo, centered at the light source, for oriented crystals, light will be deflected to both sides of the light source, giving rise to parhelia. The color of the parhelia, reddish towards the sun and bluish tails at the outside, is due to dispersion, i.e. different minimum deviation angles for the various wavelengths.

Similarly, other halos, often referred to as arcs, are due to other ray paths. A very brief survey of some common halos (today, more than 40 different types are known) is shown in Fig. 19.26. The circumzenith arc (No. 7 in Fig. 19.26) is due to rays which enter the top basal face and exit a prism face of crystals with vertical symmetry axis. For random orientation, ray paths which refer to such a 90° prism lead to circular halos of 46° (No. 3 in Fig. 19.26). Pure reflection halos – not colored, since refraction does not contribute – are e.g. sun pillars (No. 4 in Fig. 19.26). They arise when sunlight is reflected at grazing incidence from the horizontal faces of plate crystals oriented with their axes vertical. Similarly oriented crystals also give rise to the parhelic circle (No. 5 in Fig. 19.26), which is due to reflected sunlight from crystal faces lying in the vertical plane.

Singly oriented column crystals – column crystals with axes horizontal but otherwise unconstrained – give rise to the upper and lower tangent arcs. Much more rarely, column crystals orient with two prism faces horizontal. Crystals having these Parry orientations give rise to Parry arcs. Still other crystal orientation modes are possible. Furthermore, crystals occasionally have pyramidal faces that produce halos at other angular distances, referred to as odd-radius halos.

The modern theory of halos started in the 17th century [19.44, 172]. In recent decades, enormous progress has been made. This is due to computer techniques, the application of more traditional, conceptual mathematics [19.173], experiments which collected atmospheric ice crystals during observation of halo displays in cold climates, and to dedicated observers who have documented many new halos.

Probably the biggest step was made by the introduction of computer simulations which allow the computation of complex halos from many different types of crystal shapes, sizes and orientation. They gave a lot of new information, especially regarding intensity variations within a given halo [19.48, 174, 175]. Various arcs could be directly related to the crystals and the ray paths that were producing them. The theoretical displays could be easily compared with photographs or drawings of real halo displays.

Many excellent displays were documented by Finnish or German observer networks ([19.176], see

also Table 19.4) and scientists in Antarctica [19.52]. Computer simulations were also used to explain old documented displays dating back to the 18th century [19.177]. Analysis of halos also include polarization effects, started by systematic studies in the seventies [19.53, 178]. Halo polarimetric studies should allow the detection and identification of birefringent crystals in extraterrestrial atmospheres [19.179–181]. Very recently, the focus had been on comparison of observations with the simulation of halo polarization profiles, the size and shape of the crystals in the model being based on sampled ice crystals [19.182].

Halo phenomena have also been studied in the laboratory for quantitative comparison to theory and as demonstration experiments using prisms or hexagons made of glass, lucite or other materials [19.43, 66, 109, 110, 112].

19.6.7 The Color of the Sun and Sky

The Color of the Sun

Light scattering in the atmosphere is responsible for the color of the sun or moon, as perceived by earthbound observers. Outside the atmosphere, solar irradiation has a very broad spectrum, ranging from UV to the deep infrared [19.183]. Neglecting processes in the sun's atmosphere, it more or less resembles the emission of a black body of about 5900 K. This radiation is interpreted as white by human eyes (the exact color may be computed from spectra according to color metric formulae, see e.g. [19.76]). In the Earth's atmosphere, the radiation is absorbed and scattered. Compared to the outside spectrum, the irradiation curve is lowered and shows characteristic absorption features, mostly from H_2O, CO_2 and oxygen (see Fig. 19.7).

Color changes occur depending on air mass, i.e. sun elevation. Starting with a purely nonabsorbing molecular atmosphere, atmospheric transmission has been computed for air mass AM = 1 [19.3]. Therefrom the transmission at arbitrary zenith angles φ and starting at height h of an observer may be computed according

Table 19.6 Transmission of a molecular atmosphere ($h = 0$) for sun in zenith (AM = 1: $\varphi = 0°$) or close to the horizon (AM = 10: $\varphi = 85°$, AM = 38: $\varphi = 90°$), $T(\varphi = 0°)$ after [19.3]

λ(nm)	T(AM = 1)	T(AM = 10)	T(AM = 38)
630	0.945	0.625	0.117
530	0.892	0.320	0.013
430	0.764	0.068	0.000036

to [19.86, 114]

$$T(\varphi, h) = T(0, h)^{\mathrm{AM}(\varphi, h)} \qquad (19.40)$$

Results for the transmission of red ($\lambda = 630$ nm), green ($\lambda = 530$ nm) and blue ($\lambda = 430$ nm) light for a molecular atmosphere and AM = 1, ($\varphi = 0°$, zenith), AM = 10 ($\varphi \approx 85°$) and AM = 38 ($\varphi = 90°$, horizon) are given in Table 19.6.

Whereas the zenith sun is still regarded as white, the sun's spectrum near the horizon is drastically changed in favor of red and green light. Above the horizon, yellow colors may be observed and close to the horizon, red dominates. Since, simultaneously, the radiance of the sun decreases drastically, the brightness also decreases with φ. Naked-eye observations are, however, still not possible in very clear air even if $h = 0$ (sea level). In general, however, haze due to water vapor and aerosols leads to additional weakening.

Aerosols are very important for optical variations within the atmosphere [19.15, 16]. The difference of observations and theoretical spectra, including selective absorption of molecules within the air, is attributed to aerosols [19.114].

Extraordinary color changes of the sun can sometimes occur, if clouds of nearly uniformly sized particles are present in the line of sight. For example, the forest fires in Canada in 1950 ejected large numbers of oil droplets in the air. These were transported over long distances and led to blue sun observations even in Edinburgh [19.74, 184]. Similar events may be due to volcanic eruptions.

Sky Colors

Obviously, sky colors are due to many factors [19.43–49, 51]. A simple qualitative explanation of typical sky colors at sunset can be given according to Fig. 19.27.

Fig. 19.27 Geometry for qualitative explanation of sky colors after sunset (see text for details)

The sun has just set, i. e. it is below the horizon. Sunlight still illuminates portions of the atmosphere. The color that an observer perceives in a given direction is due to contributions of scattered and attenuated light along a line of sight in the respective direction. In simple terms, the amount of radiation entering the observers eye depends on, first, the light path through the atmosphere before scattering, second, the height of the scattering event, which determines the density of scatterers, third, the scattering angle, and fourth, the optical thickness along the line of sight, i. e. the attenuation due to scattering and/or absorption. The subtle interplay of these four parameters determines the spectrum of light reaching the eye of an observer and hence the perceived color.

Different locations along the line of sight will contribute to the scattered light with varying intensity as well as spectral composition. The light beam most distant from the Earth will reach the line of sight, nearly unattenuated, and a broad spectrum is available for scattering. Due to the large height, only a small amount of radiation is scattered towards the observer, with blue dominating. This light is further attenuated before reaching the observer. The final spectral composition of the light depends on the optical thickness that must be traversed. However, blue is most strongly attenuated, i. e. overall this light will not contribute much and will not dominate the color. The closer the light passes to the ground, the more its spectrum is shifted towards the red. Although less light will intersect the line of sight compared to the large height rays, it will contribute more, since it interacts at lower heights, i. e. with a much larger density of scatterers. Taking into account the further shift of the scattered light spectrum towards the red due to scattering along the line of sight shows that the sky color will be dominated by yellowish and red colors.

The brightness and color of the clear sky has also been investigated for various zenith angles φ [19.185]. For high sun elevations, the zenith sky of a pure Rayleigh atmosphere is blue (as observed for clear air), however, it would turn yellowish after sunset. This is in contrast to the observed blue color. The solution of this puzzle are the Chappuis absorption bands of ozone in the wavelength range between 500 and 700 nm. For high sun elevations, the ozone absorption contribution to sky light is small compared to Rayleigh scattering whereas it dominates for very low sun elevations.

Aerosols within the atmosphere are usually not distributed homogeneously, but in the form of ac-cumulations, carried by the wind, thus undergoing constant qualitative changes, including condensation processes [19.114]. As a consequence, the extinction coefficient for various atmospheric compositions, e.g., for different types of clouds, and low- or high-altitude haze varies considerably [19.76]. For simplicity, let us now assume just a single aerosol layer. Its influence on sky colors is simply to intensify the red and yellow colors in the forward direction. This is due to the fact that the scattering angles are rather small and that aerosol particles show very strong forward scattering, compared to Rayleigh scattering (Fig. 19.17).

Similar qualitative arguments may also be applied to the phenomenon of the so-called blue mountains. During the day, the sky is illuminated by the sun. If the line of sight to a distant mountain is close to the horizon, the radiation entering the eye of an observer is due to two contributions. First, it consists of the light originally scattered by the mountain towards the observer. This light is attenuated due to scattering along the line of sight. Second, the observer will see sunlight that is scattered by the air along the line of sight. This air light will be blue in a Rayleigh atmosphere. Observing a scenery with mountains at various distances will change the amount of the two contributions: the more distant, the smaller the first will be and the more important the second contribution (see the discussion on visibility in Sect. 19.6.8). As a consequence, distant objects will appear to have a faint blue color [19.45, 51]. This scheme can be used to get a measure for the thickness of the atmosphere [19.186].

Very often, one observes that sky light close to the horizon is whitish. This can be understood in a similar way. Since no objects except the sky are observed, the first contribution from the above argument vanishes and only air light has to be considered. Sunlight which is scattered in a length interval close to the observer contributes a large amount of blue light due to Rayleigh scattering at low heights above the ground. Light which is scattered at larger distances from the observer is scattered at larger heights, i. e. contributes smaller amounts of predominantly blue light. In addition this light is attenuated and spectrally modified by additional scattering along the line of sight. As a result, light which originates far from the observer contributes small amounts of multiply scattered mostly red light. All contributions along the line of sight add up to give an overall white color. Since light from distant portions will cease to contribute if scattered out of the line of sight, the overall brightness has a limit [19.45, 51, 77].

Observations from Mauna Loa of the polarization and color ratio during twilight often show deviations from the clear-sky average. These were attributed to cloud or haze shadow effects and the importance of stratospheric dust layers was emphasized [19.187]. Stratospheric dust clouds from volcanic eruptions do strongly affect the degree of polarization of sky light and also shift the positions of neutral points by more than 15° [19.188]. Such investigations strongly profit from the development of LIDAR systems and the respective theories of backscattering from small particles [19.189–192].

Modern experiments simultaneously measure the sky light radiance distribution at three wavelengths, the degree of polarization, and the plane of polarization [19.193]. Recently, the color coordinates of sky light have been investigated, showing that sky light colors have a wide range of chromaticity curves, depending strongly on location. Sometimes difficulties arise in separating luminance changes from chromaticity changes [19.194]. Astonishingly, clear daytime skies show a local maximum of radiance near the astronomical horizon. Its angular width and elevation vary with the solar elevation, azimuth relative to the sun, and aerosol optical depth. This is understood in terms of second-order scattering processes [19.195].

When the sun is seen through thin clouds, it usually has a sharp edge, but occasionally is fuzzy. This is due to certain clouds with ranges of cloud optical thicknesses depending on the cloud particle sizes [19.196].

Present investigations of sky light deal, e.g., with digital imaging of clear-sky polarization [19.197], twilight modeling [19.198] as well as color and luminance asymmetries in clear [19.199] and overcast [19.200] skies. Sky light measurements have also been reported for Mars, based on data from the Viking and Pathfinder missions. The Martian atmosphere has a high dust-particle content resulting in very high sky brightness and the sky colors vary strongly with the angular position of the sun [19.201].

Theoretical modeling of atmospheric extinction greatly profited from computer technology. Nowadays, the transmission of the atmosphere is modeled by extensive databases. The most prominent of these are the HITRAN and LOWTRAN databases [19.76, 202]. In particular, the LOWTRAN program calculates the transmission spectrum for molecular absorption, Rayleigh scattering and aerosol extinction at a moderate resolution of $20\,\mathrm{cm}^{-1}$.

19.6.8 Clouds and Visibility

Clouds

Clouds are visible aggregates of water droplets or ice crystals, suspended in the air and grown around condensation nuclei [19.118]. Fog or clouds have droplet sizes around or above $10\,\mu\mathrm{m}$, with densities ranging from 10 to 1000 droplets/cm^3. On average we will assume 300 droplets/cm^3 [19.203]. Droplets of $5-10\,\mu\mathrm{m}$ radius will then correspond to volume fractions f of about $10^{-7}-10^{-6}$.

Clouds exhibit several optical phenomena, the most obvious being their white color, but certain types of clouds show particular phenomena. Cirrus and cirrustratus clouds may give rise to coronas, iridescence and halos, contrails of aircraft engines are cirrus-like trails of condensed vapor with characteristics similar to cirrus clouds, and cumulonimbus clouds relate to thunderstorms, i. e. lightning. Here, the color of clouds, their absorption and extinction will be briefly discussed. The effect of photon path length distributions within clouds is discussed in the contribution of *U. Platt* and *K. Pfeilsticker* (Sect. 19.5.5).

If illuminated by white light, clouds appear white (lower brightness is often interpreted as grey or dark). Since water droplets are mostly nonabsorbing in the visible, the color must be due to scattering. Scattering of light from monodisperse water droplets of about $10\,\mu\mathrm{m}$ shows Ripple structures (Fig. 19.16) [19.40,41], for size distributions this is washed out and scattering is mostly independent of wavelength in the visible spectral range. Although this is a sufficient condition for clouds to be white, it is not necessary [19.204]. As a matter of fact, a suspension of Rayleigh scatterers (such as fat droplets in milk), i. e. selective scatterers, also give a white color due to multiple scattering.

The criterion for multiple scattering to take place is that the optical thickness τ is large compared to unity. A molecular atmosphere had $\tau < 1$, therefore the explanation of the blue sky needs only single scattering events. For clouds, τ for a distance x can be estimated by the following argument: within clouds, the extinction coefficient is more or less constant, hence $\tau = \beta x$. The extinction coefficient β can be estimated from Mie theory calculations. Droplets of about $10\,\mu\mathrm{m}$ in diameter have extinction cross sections of about twice the geometrical cross section (this is the extinction paradox, [19.41]), i. e. of the order of $10^{-6}\,\mathrm{cm}^2$. For concentrations of 300/cm^3, this leads to extinction

coefficients β of the order of $0.05\,\mathrm{m}^{-1}$. A very simple estimate [19.77] can also be made by starting from $\beta = N\sigma$ and substituting the number density N by the volume fraction $f \approx N\varnothing^3$ and the cross section by approximately the geometrical cross section $\sigma \approx \varnothing^2$ to find

$$\beta \approx f/\varnothing \tag{19.41}$$

for $f = 10^{-6}$ and 10-µm particles, this also gives the order of $0.1/\mathrm{m}$.

Hence, a cloud of several meters thickness corresponds to the optical thickness of the whole normal atmosphere. The transmission is given by $T = \mathrm{e}^{-\beta x}$ and for $\beta = 0.05\,\mathrm{m}^{-1}$ a distance of 20 m leads to $\tau = 1$ ($T = 1/\mathrm{e}$), $x = 100\,\mathrm{m}$ to $\tau = 5$ ($T \approx 7\times10^{-3}$), and $x = 200\,\mathrm{m}$ to $\tau = 10$ ($T \approx 5\times10^{-5}$), which is sufficient to obscure the disk of the sun [19.77]. Low transmission automatically leads to high reflection, i.e. thick clouds have a high albedo which explains the bright white color observed from airplanes above clouds. In conclusion, multiple scattering dominates for any cloud that is optically thick and composed of nearly nonabsorbing particles; upon illumination by white light it will look white. The color of clouds may change during sunrise and sunset if spectrally filtered light illuminates the clouds, giving rise to spectacular sceneries.

The very small transmission of sunlight through thick clouds also accounts for the fact that the bases of such clouds are usually very dark. If droplets near the base grow to form raindrops, the extinction coefficient changes. The volume fraction stays about the same, but raindrops have a size of, say, 1 mm, hence β in a rain shower is about a factor 100 smaller than within the clouds. This explains, why it is easily possible to look through very heavy rainfalls.

Visibility

Visibility is a measure of how far one can see through the air. Even in the clearest air – assuming that no aerosol particles are present and that one is not restricted by the Earth's curvature – the horizontal visibility is limited to a few hundred kilometers. This is due to the scattering and absorption of the components of the air (vertically, the atmosphere is optically much thinner, hence we may see the stars at night). In meteorology, visibility refers to the observation of distant dark objects against a bright background, usually the sky. The basis for a theoretical derivation [19.77, 205–209] is the contrast ratio C, giving the normalized difference between the background intensity of the object and the intensity of the air light from the line of sight. One finds for the resulting maximum distance D

$$D = -\ln(C)/\beta , \tag{19.42}$$

where β is the scattering coefficient. The sensitivity of the human eye has a maximum at $\lambda = 555\,\mathrm{nm}$, therefore one usually evaluates (19.42) for green light. D then just depends on the threshold contrast C, i.e. the lowest visual brightness contrast, a person can see. It is common to assume $C = 0.02$ although it varies from individual to individual. This gives $D = 3.912/\beta$. Values of D for various β are shown in Table 19.7. Obviously, there is an enormous range of distances from several meters in dense fog to several hundred kilometers in very clear air. Hence, the visibility is an indicator of the aerosol and/or water droplet content.

19.6.9 Miscellaneous

There is a great number of other optical phenomena associated with the atmosphere. In the following, these will be very briefly described and references will be given.

Green flashes or green suns are phenomena when either the last rays at sunset or the first rays at sunrise look green or when, at low sun elevations, the upper rim of the sun looks green. In the first case, just a very small portion of the sun is above the horizon, in the second case, the sun's disk is usually highly distorted due to mirage effects. The explanations of these phenomena require refraction and the scattering of the sunlight as well as mirage effects [19.103, 210, 211].

Noctilucent clouds are blue, white or silvery looking clouds within the stratosphere at heights of about 80 km

Table 19.7 Typical values for visibility in molecular atmosphere and examples if aerosols (natural/anthropogenic) and water droplets are present

	β	D	
Molecular atmosphere	$0.013\,\mathrm{km}^{-1}$	300 km	Extremely excellent visibility
Some particles	$0.050\,\mathrm{km}^{-1}$	80 km	Excellent visibility
Many particles	$0.500\,\mathrm{km}^{-1}$	8 km	Poor visibility
Thick fog	$0.050\,\mathrm{m}^{-1}$	80 m	Extremely poor visibility

which can still be illuminated by sunlight 1–2 h after sunset [19.212–214]. They often show wavelike features with wavelengths in the range from 1–100 km.

Interesting colorful phenomena may be observed during eclipses. For example, the colors and brightness of lunar eclipses are directly related to the scattering of sunlight within the Earth's atmosphere [19.215, 216]. Other examples include polarization of sky light [19.217, 218], twilight phenomena [19.219], and illuminance measurements [19.220] during solar eclipses.

Shadows are regions in space that are shielded from light. They give rise to very prominent daily-life phenomena in atmospheric optics such as the crepuscular rays, sometimes called sun beams or shadow beams [19.45,48,51,221] or the fact that mountain shadows are always triangular, irrespective of the contour of the mountain [19.222, 223].

A very personal experience, based on our visual system, is the so-called moon illusion, i. e. the fact that the sun or the moon looks much bigger near the horizon than when it is higher in the sky [19.224, 225]. This phenomenon is not reproduced on photos.

In addition to phenomena with external light sources such as the sun, moon or stars, a number of optical phenomena in the atmosphere produce light. The most well known are auroras, multicolored, diffuse and slowly moving lights, usually seen only in high altitudes against the clear dark night sky. They are due to air molecules and atoms, which are excited by collisions with electrons from the solar wind [19.51, 226, 227]. At times of increased solar activity, they may also be observed at low latitudes. These events are accurately predictable, since the solar wind needs time to reach the Earth (see the websites on space weather in Table 19.4).

Lightning, one of the most common and spectacular natural phenomena, is due to electric charging effects in thunderstorm clouds. The exact microphysical processes that are responsible for the charging are still under dispute [19.228–230]. Recent research has revealed a whole new class of phenomena: lightning-related transient luminous events (TLE), including sprites, blue jets, elves, trolls etc. [19.231]. These TLE extend from the top of thunderclouds at heights of up to 100 km and raise serious questions about possible hazards for aerospace operations. In addition, promising efforts are under way concerning lightning protection by initiation of the discharge using intense femtosecond lasers [19.232].

Meteors are sometimes faint, sometimes brilliant streaks of light with luminous trails in the night sky. Meteor incorporates all phenomena when a cosmic particle enters the atmosphere. Outside the atmosphere, they are called meteoroids and, if they reach ground, meteorites. The visual effects are due to heating of particles in the atmosphere due to frictional forces. Small particles heat up until they evaporate. Thereby, they collide with air molecules and ionize a channel of air. Light is then emitted upon recombination [19.233, 234].

References

19.1 Lord Rayleigh, J. W. Strutt: On the transmission of light through an atmosphere containing small particles in suspension and on the origin of the blue of the sky, Philos. Mag. **XLVII**, 375–384 (1899)

19.2 M. Nicolet: On the molecular scattering in the terrestrial atmosphere: An empirical formula for its calculation in the homosphere, Planet. Space Sci. **32**, 1467–1468 (1984)

19.3 R. Penndorf: Tables of the refractive index for standard air and the Rayleigh scattering coefficient for the spectral region between 0.2 and 20 μm and their application to atmospheric optics, J. Opt. Soc. Am. **47**, 176–182 (1957)

19.4 M. Bussemer: Der Ring-Effekt: Ursachen und Einfluß auf die spektroskopische Messung stratosphärischer Spurenstoffe Ph.D. Thesis (Univ. Heidelberg, Heidelberg 1993)

19.5 J. Burrows, M. Vountas, H. Haug, K. Chance, L. Marquard, K. Muirhead, U. Platt, A. Richter, V. Rozanov: *Study of the Ring Effect*, Final Report European Space Agency (ESA), Noordvijk, The Netherlands, Contract 109996/94/NL/CN (1995)

19.6 H. Haug, K. Pfeilsticker, U. Platt: Vibrational Raman scattering in the atmosphere, (1996) unpublished

19.7 C. E. Sioris, W. F. J. Evans: Filling in of Fraunhofer and gas-absorption lines in sky spectra as caused by rotational Raman scattering, Appl. Opt. **38**, 2706–2713 (1999)

19.8 H. W. Schrötter, H. W. Klöckner: Raman scattering cross-sections in gases. In: *Raman Spectroscopy of Gases and Liquids*, ed. by A. Weber (Springer, Berlin, Heidelberg 1979)

19.9 D. Clarke, H. M. Basurah: Polarisation measurements of the ring effect in the daytime sky, Planet. Space. Sci. **37**, 627–630 (1989)

19.10 G. Mie: Beiträge zur Optik trüber Medien, speziell kolloidaler Metalllösungen, Ann. Phys. **25**, 377–445 (1908) in German

19.11 H. C. Van de Hulst: *Multiple Light Scattering, Tables, Formulas and Applications*, Vol. 1,2 (Academic, London 1980)

19.12   W. J. Wiscombe: Improved Mie scattering algorithms, Appl. Opt. **19**, 1505–1509 (1980)

19.13   R. G. Isaacs, W.-C. Wang, R. D. Worsham, S. Goldberg: Multiple scattering lowtran and fascode models, Appl. Opt. **26**, 1272–1281 (1987)

19.14   O. Funk: Photon path length distributions for cloudy skies; Oxygen a–band measurements and radiative transfer calculations Ph.D. Thesis (Univ. Heidelberg, Heidelberg 2000)

19.15   A. Angström: On the atmospheric transmission of sun radiation and on dust in the air, Geogr. Annal. Stockholm **11**, 156–166 (1929)

19.16   A. Angström: On the atmospheric transmission of sun radiation and on dust in the air, Geografiska Annal. **12**, 130 (1930)

19.17   C. E. Junge: *Air Chemistry and Radioactivity*, Vol. 4 (Academic, New York 1963)

19.18   C. E. Junge, J. E. Manson: Stratospheric aerosols studies, J. Geophys. Res. **66**, 2163–2182 (1961)

19.19   M. Milankovitch: *Canon of Insolation and the Ice-Age Problem*, Royal Serbian Acad. Sp. Pub., Vol. 132 (Royal Serbian Acad., Belgrade, Yugoslavia 1941)

19.20   J. T. Houghton, Y. Ding, D. J. Griggs, M. Noguer, P. J. van der Linden, X. Dai, K. Maskell, C. A. Johnson (Eds.): *Climate Change 2001: The Scientific Basis, published for Intergovernmental Panel on Climate Change (IPCC)* (Cambridge Univ. Press., Cambridge 2001)

19.21   S. Twomey: Pollution and the planetary albedo, Atmos. Environ. **8**, 1251–1256 (1974)

19.22   B. A. Wielicki, T. Wong, R. P. Allan, A. Slingo, J. T. Kiehl, B. J. Soden, C. T. Gordon, A. Levin, J. Miller, S.-K. Yang, D. A. Randall, F. Robertson, J. Susskind, H. Jacobowitz: Evidence for Large Decadal Variability in the Tropical Mean Radiative Energy Budget, Science **295**, 841–844 (2002) Issue 5556

19.23   D. Perner, U. Platt, M. Trainer, G. Huebler, J. W. Drummond, W. Junkermann, J. Rudolph, B. Schubert, A. Volz, D. H. Ehhalt, K. J. Rumpel, G. Rumpel, G. Helas: Tropospheric OH concentrations: A comparison of field data with model predictions, J. Atmos. Chem. **5**, 185–216 (1987)

19.24   M. W. Sigrist (Ed.): *Air Monitoring by Spectroscopic Techniques*, Chemical Analysis Series, Vol. 127 (Wiley, New York 1984)

19.25   U. Platt: Modern methods of the measurement of atmospheric trace gases, J. Phys. Chem. Chem. Phys. 'PCCP' **1**, 5409–5415 (1999)

19.26   U. Platt, D. Perner: *Measurements of atmospheric trace gases by long path differential UV/visible absorption spectroscopy: Optical and Laser Remote Sensing*, ed. by D. K. Killinger, A. Mooradien, Springer Ser. Opt. Sci. **39**, 95–105 (1983)

19.27   U. Platt: *Differential optical absorption spectroscopy (DOAS), Air Monitoring by Spectroscopic Techniques*, Chemical Analysis Series, Vol. 127, ed. by M. W. Sigrist (Wiley, New York 1994) pp. 27–84

19.28   R. Volkamer, T. Etzkorn, A. Geyer, U. Platt: Correction of the oxygen interference with UV spectroscopic (DOAS) measurements of monocyclic aromatic hydrocarbons in the atmosphere, Atmos. Environ. **32**, 3731–3747 (1998)

19.29   J. P. Burrows, E. Hölzle, A. P. H. Goede, H. Visser, W. Fricke: SCIAMACHY – Scanning imaging absorption spectrometer for atmospheric chartography, Acta Astronautica **35**(7), 445–451 (1995)

19.30   J. P. Burrows, M. Weber, M. Buchwitz, V. V.. Rozanov, A. Ladstätter-Weissenmayer, A. Richter, R. De Beek, R. Hoogen, K. Bramstedt, K.-U. Eichmann, M. Eisinger: The global ozone monitoring experiment (GOME): Mission concept and first scientific results, J. Atmos. Sci. **56**, 151–175 (1999)

19.31   R. Volkamer, P. Spietz, J. P. Burrows, U. Platt: High-resolution absorption cross-section of Glyoxal in the UV/vis and IR spectral ranges, J. Photochem. and Photobiol. A: Chemistry **172**, 35–46 (2005) DOI: 10.1016/j.jphotochem.2004.11.011

19.32   C. Weitkamp (ed.): *Lidar – Range-Resolved Optical Remote Sensing of the Atmosphere* (Springer, Berlin, Heidelberg, New York 2005)

19.33   S. Nyeki, K. Eleftheriadis, U. Baltensperger, I. Colbeck, M. Fiebig, A. Fix, C. Kiemle, M. Lazaridis, A. Petzold: Airborne Lidar and in-situ aerosol observations of an elevated layer, Leeward of the European Alps and Apennines, Geophys. Res. Lett. **29**, 1852 (2002) doi:10.1029/2002 GL 014897

19.34   K. Pfeilsticker, F. Erle, O. Funk, H. Veitel, U. Platt: First geometrical path lengths probability density function derivation of the skylight from spectroscopically highly resolving oxygen A-band observations, 1. Measurement technique, atmospheric observations, and model calculations, J. Geophys. Res. **103**, 11483–11504 (1998)

19.35   K. Pfeilsticker: First geometrical path lengths probability density function derivation of the skylight from spectroscopically highly resolving oxygen A-band observations. 2. Derivation of the Lévy-index for the skylight transmitted by mid-latitude clouds, J. Geophys. Res. **104**, 4101–4116 (1999)

19.36   V. Veitel, O. Funk, C. Kurz, U. Platt, K. Pfeilsticker: Geometrical path length probability density function of the skylight transmitted by mid-latitude cloudy skies; Some case studies, Geophys. Res. Lett. **25**, 3355–3358 (1998)

19.37   Q.-L. Min, L. C. Harrison, E. Clothiaux: Joint statistics of photon path length and cloud optical depth: Case studies, J. Geophys. Res. **106**, 7375–7386 (2001)

19.38   O. Funk, K. Pfeilsticker: Photon path lengths distributions for cloudy skies: Oxygen A-band measurements and model calculations, Annal. Geophysicae **21**, 615–626 (2003)

19.39   C. Savigny, O. Funk, U. Platt: Radiative Smoothing in zenith-scattered skylight transmitted to the ground, Geophys. Res. Lett. **26**, 2949–2952 (1999)

19.40 H. C. van de Hulst: *Light Scattering by Small Particles* (Dover, New York 1981)

19.41 C. F. Bohren, D. R. Huffman: *Absorption and Scattering of Light by Small Particles* (Wiley, New York 1983)

19.42 U. Kreibig, M. Vollmer: *Optical Properties of Metal Clusters*, Springer Ser. Mat. Sci., Vol. 25 (Springer, Berlin, Heidelberg 1995)

19.43 M. Vollmer: *Lichtspiele in der Luft–Atmosphärische Optik für Einsteiger* (Spektrum–Elsevier, Heidelberg 2006)

19.44 J. M. Pernter, F. M. Exner: *Meteorologische Optik*, 2nd edn. (Braumüller, Wien 1922)

19.45 M. G. J. Minnaert: *Light and Color in the Outdoors*, 1 edn. (Springer, Berlin, Heidelberg 1993) in Dutch 1937

19.46 W. J. Humphreys: *Physics of the Air* (Dover, New York 1963) p. 1929 reprint

19.47 R. A. R. Tricker: *Introduction to Meteorological Optics* (Elsevier, New York 1970)

19.48 R. Greenler: *Rainbows, Halos, and Glories* (Cambridge Univ. Press, Cambridge 1980)

19.49 A. Meinel, M. Meinel: *Sunsets, Twilights, and Evening Skies* (Cambridge Univ. Press, Cambridge 1983)

19.50 C. F. Boyer: *The Rainbow: From Myth to Mathematics* (Princeton Univ. Press, Princeton 1987) revised printing

19.51 D. K. Lynch, W. Livingston: *Color and Light in Nature*, 2 edn. (Cambridge Univ. Press, Cambridge 2001)

19.52 W. Tape: *Atmospheric Halos* (Am. Geophys. Soc., Washington 1994)

19.53 G. P. Können: *Polarized Light in Nature* (Cambridge Univ. Press, Cambridge 1985)

19.54 R. Lee, A. B. Fraser: *The Rainbow Bridge* (Penn. State Press, University Park 2001)

19.55 C. F. Bohren (Ed.): *Selected papers on Scattering in the Atmosphere*, SPIE Milestone Series MS7 (SPIE, Bellingham 1989)

19.56 OSA (ed): *Proceedings of 1st conference on atmospheric optics*, J. Opt. Soc. Am., Vol. 68 (Optical Society of America, Washington, D.C. 1979)

19.57 OSA (ed): *Proceedings of 2nd conference on atmospheric optics*, J. Opt. Soc. Am., Vol. 73 (Optical Society of America, Washington, D.C. 1983)

19.58 OSA (ed): *Proceedings of 3rd conference on atmospheric optics*, Vol. 4 (Optical Society of America, Washington, D.C. 1987)

19.59 OSA (ed): *Proceedings of 4th conference on atmospheric optics*, Appl. Opt., Vol. 30 (Optical Society of America, Washington, D.C. 1991)

19.60 OSA (ed): *Proceedings of 5th conference on atmospheric optics*, Appl. Opt., Vol. 33 (Optical Society of America, Washington, D.C. 1994)

19.61 OSA (ed): *Proceedings of 6th conference on atmospheric optics*, Appl. Opt., Vol. 37 (Optical Society of America, Washington, D.C. 1998)

19.62 OSA (ed): *Proceedings of 7th conference on atmospheric optics*, Appl. Opt., Vol. 42 (Optical Society of America, Washington, D.C. 2003)

19.63 OSA (ed): *Proceedings of 8th conference on atmospheric optics*, Appl. Opt., Vol. 44 (Optical Society of America, Washington, D.C. 2005)

19.64 C. L. Adler (Ed.): *On Minnaert's Shoulders: Twenty Years of the Light and Color Conferences*, Vol. 1 (Opt. Soc. Am., Washington 1999) Classic Preprints on CD-ROM

19.65 R. Greenler: *The Mirage, the Discovery of Greenland and the Green Flash*, video available from www.blueskyassociates.com

19.66 R. Greenler: *Sunlight and Ice Crystals in the Skies of Antarctica*, video available from www.blueskyassociates.com

19.67 R. Greenler: *Red Sunsets, Black Clouds and the Blue Moon: Light Scattering in the Atmosphere*, video available from www.blueskyassociates.com

19.68 M. Engler: *Fata Morganen–Zauberspiegel am Horizont*, German TV film first broadcast 1996 by French–German TV program ARTE

19.69 M. Engler: *Fata Morgana–Naturwunder und Zauberspuk*, German TV film first broadcast 2001 by French–German TV program ARTE

19.70 S. Gedzelman: Atmospheric optics in art, Appl. Opt. **30**, 3514 (1991)

19.71 S. Rother: *Der Regenbogen, eine malereigeschichtliche Studie* (Böhlau, Köln 1992) in German

19.72 K. Sassen: Rainbows in the Indian rock art of desert western America, Appl. Opt. **30**, 3523 (1991)

19.73 K. Sassen: Possible halo depictions on the prehistoric rock art of Utah, Appl. Opt. **33**, 4756 (1994)

19.74 C. F. Bohren: *Clouds in a Glass of Beer* (Wiley, New York 1987)

19.75 E. A. Wood: *Science from your Airplane Window* (Dover, New York 1975) 1st edn. 1968

19.76 M. Bass: *Handbook of Optics*, Vol. 1, ed. by E. van Stryland, D. Williams, W. Wolfe (McGraw Hill, New York 1995)

19.77 C. F. Bohren: Atmospheric optics, Encyclop. Appl. Phys. **12**, 405 (1995)

19.78 Lord Rayleigh, J. W. Strutt: On the light from the sky, its polarization and colour, Philos. Mag. **XLI**, 107, 274 (1871)

19.79 A. T. Young: Rayleigh scattering, Phys. Today **35**, 42–48 (1982)

19.80 G. Hoeppe: *Blau – Die Farbe des Himmels* (Spektrum Akad. Verlag, Heidelberg 1999) in German

19.81 K. Bullrich: Scattered radiation in the atmosphere and the natural aerosol, Adv. Geophys. **10**, 99 (1964)

19.82 S. Twomey: *Atmospheric Aerosols* (Elsevier, Amsterdam 1977)

19.83 T. E. Graedel, P. J. Crutzen: *Atmospheric Change: An Earth System Perspective* (Freeman, New York 1993)

19.84 E. Hecht: *Optics*, 3 edn. (Addison Wesley, San Francisco 1998)

19.85   F. Kasten, A. T. Young: Revised optical air mass tables and approximation formula, Appl. Opt. **28**(22), 4735–4738 (1989)

19.86   M. Vollmer, S. D. Gedzelman: Colours of the sun and moon: the role of the optical air mass, Eur. J. Phys. **27**, 299–306 (2006)

19.87   G. H. Liljequist, K. Cehak: *Allgemeine Meteorologie* (Vieweg, Braunschweig 1984) in German

19.88   Z. Néda, S. Volkán/Kacsó: Flatness of the setting sun, Am. J. Phys. **71**, 379–385 (2003)

19.89   A. I. Mahan: Astronomical refraction–some history and theories, Appl. Opt. **1**, 497–511 (1962)

19.90   A. D. Wittmann: Astronomical refraction:formulas for all zenith distances, Astron. Nachr. **318**(5), 305–312 (1997)

19.91   L. K. Kristensen: Astronomical refraction and air-mass, Astron. Nachr. **318**(3), 193–198 (1998)

19.92   A. T. Young: Air mass and refraction, Appl. Opt. **33**(6), 1108–1110 (1994)

19.93   A. Wegener: Elementare Theorie der atmosphärischen Spiegelungen, Ann. Phys. **57**, 203 (1918) in German

19.94   W. H. Lehn: A simple parabolic model for the optics of the atmospheric surface layer, Appl. Math. Model. **9**, 447 (1985)

19.95   W. H. Lehn, T. L. Legal: Long range superior mirages, Appl. Opt. **37**, 1489 (1998)

19.96   E. Tränkle: Simulation of inferior mirages observed at the Halligen sea, Appl. Opt. **37**, 1495 (1998)

19.97   A. T. Young, G. W. Kattawar, P. Parviainen: Sunset science 1. The mock mirage, Appl. Opt. **36**, 2689 (1997)

19.98   A. T. Young, G. W. Kattawar: Sunset science I1. A useful diagram, Appl. Opt. **37**, 3785 (1998)

19.99   W. H. Lehn: The Novaya Zemlya effect: An artic mirage, J. Opt. Soc. Am. **69**, 776 (1979)

19.100   W. H. Lehn, B. A. German: Novaya Zemlya effect: Analysis of an observation, Appl. Opt. **20**, 2043 (1981)

19.101   S. Y. van der Werf, G. P. Können, W. H. Lehn: Novaya Zemlya effect and sunsets, Appl. Opt. **42**, 367 (2003)

19.102   S. Y. van der Werf, G. P. Können, W. H. Lehn, F. Steenhuisen, W. P. S. Davidson: Gerrit de Veers's true and perfect description of the Novaya Zemlya effect, 24–27 January 1957, Appl. Opt. **42**, 379 (2003)

19.103   A. B. Fraser: The green flash and clear air turbulence, Atmosphere **13**, 1 (1975)

19.104   W. H. Lehn, W. K. Silvester, D. M. Fraser: Mirages with atmospheric gravity waves, Appl. Opt. **3**, 4639 (1994)

19.105   S. Y. van der Werf: Ray tracing and refraction in the modified US 1976 atmosphere, Appl. Opt. **42**, 354 (2003)

19.106   R. D. Sampson, E. P. Lozowski, A. E. Peterson: Comparison of modeled and observed astronomical refraction of the setting sun, Appl. Opt. **42**, 342 (2003)

19.107   W. H. Lehn: Bright superior mirages, Appl. Opt. **42**, 390 (2003)

19.108   R. Greenler: Laboratory simulation of inferior and superior mirages, J. Opt. Soc. Am. A **4**, 589 (1987)

19.109   M. Vollmer: Atmospheric Optics, Topical Issue, Prax. Naturwiss. Phys. **3**, 46 (1997) in German

19.110   M. Vollmer, R. Tammer: Laboratory experiments in atmospheric optics, Appl. Opt. **37**, 1557 (1998)

19.111   C. Tape: Aquarium, computer, and Alaska range mirages, The Physics Teacher **38**, 308 (2000)

19.112   M. Vollmer, R. Greenler: Halo and mirage demonstrations in atmospheric optics, Appl. Opt. **42**, 394 (2003)

19.113   J. M. Palmer: Getting intense on intensity, Metrologia **30**, 371–372 (1993)

19.114   G. V. Rozenberg: Light scattering in the Earth's atmosphere, Sov. Phys. Uspekhi **3**, 346 (1960)

19.115   J. A. McDonald: The shape and aerodynamics of large raindrops, J. Meteorol. **11**, 478 (1954)

19.116   A. W. Green: An approximation for the shapes of large raindrops, J. Appl. Meteorol. **14**, 1578 (1975)

19.117   K. V. Beard, H. T. Ochs III, R. J. Kubesh: Natural oscillations of small raindrops, Nature **342**, 408 (1989)

19.118   H. R. Pruppacher, J. D. Klett: *Microphysics of Clouds and Precipitation* (Kluwer, Dordrecht 1997)

19.119   P. L. Marston: Rainbow phenomena and the detection of nonsphericity in drops, Appl. Opt. **19**, 680 (1980)

19.120   G. P. Können: Appearance of supernumeraries of the secondary rainbow in rain showers, J. Opt. Soc. Am. A **4**, 810 (1987)

19.121   R. W. Wood: *Physical Optics*, 3 edn. (Macmillan, New York 1934)

19.122   J. Walker: Multiple rainbows from single drops of water and other liquids, Am. J. Phys. **44**, 421 (1976)

19.123   J. Walker: How to create and observe a dozen rainbows in a single drop of water, Sci. Am. **237**, 138 (1977)

19.124   J. Walker: Mysteries of rainbows, notably their rare supernumerary arcs, Sci. Am. **240**, 146 (1980)

19.125   J. A. Lock: Theory of observations made of high-order rainbows from a single water droplet, Appl. Opt. **26**, 5291 (1987)

19.126   H. M. Nussenzveig: The theory of the rainbow, Sci. Am. **4**, 116 (1977)

19.127   G. B. Airy: On the intensity of light in the neighborhood of a caustic, Trans. Cambridge Philos. Soc. **VI**, 397 (1838)

19.128   G. B. Airy: On the intensity of light in the neighborhood of a caustic, Appendum **VIII**, 595 (1849)

19.129   H. M. Nussenzveig: Complex angular momentum theory of the rainbow and the glory, J. Opt. Soc. Am. **69**, 1068 (1979)

19.130   M. V. Berry, C. Upstill: Catastrophe optics: Morphologies of caustics and their diffraction patterns, Prog. Opt. **18**, 257 (1980)

19.131   D. K. Lynch, P. Schwartz: Rainbows and fogbows, Appl. Opt. **30**, 3415 (1991)

19.132 R. T. Wang, H. C. van de Hulst: Rainbows: Mie computations and the Airy approximation, Appl. Opt. **30**, 106 (1991)

19.133 J. A. Adam: The mathematical physics of rainbows and glories, Phys. Rep. **356**, 229–365 (2002)

19.134 A. B. Fraser: Why can the supernumerary bows be seen in a rain shower?, J. Opt. Soc. Am. **73**, 1626 (1983)

19.135 J. A. Lock: Observability of atmospheric glories and supernumerary rainbows, J. Opt. Soc. Am. A **6**, 1924 (1989)

19.136 J. A. Lock: *Review on rainbow phenomena*, as introduction to rainbows in [19.64]

19.137 S. D. Gedzelman: Rainbows in strong vertical atmospheric electric fields, J. Opt. Soc. Am. A **5**, 1717 (1988)

19.138 S. D. Gedzelman: Visibility of halos and rainbows, Appl. Opt. **19**, 3068–3074 (1980)

19.139 S. D. Gedzelman: Rainbow brightness, Appl. Opt. **21**, 3032–3037 (1982)

19.140 R. Greenler: Infrared rainbow, Science **173**, 1231 (1971)

19.141 K. Sassen: Angular scattering and rainbow formation in pendent drops, J. Opt. Soc. Am. **69**, 1083 (1979)

19.142 P. H. Ng, M. Y. Tse, W. K. Lee: Observation of high-order rainbows formed by a pendent drop, J. Opt. Soc. Am. B **15**, 2782 (1998)

19.143 D. S. Langley, P. L. Marston: Generalized tertiary rainbow of slightly oblate drops: Observations with laser illumination, Appl. Opt. **37**, 1520 (1998)

19.144 C. L. Adler, J. A. Lock, B. R. Stone: Rainbow scattering by a cylinder with nearly elliptical cross section, Appl. Opt. **37**, 1540 (1998)

19.145 J. A. Lock, C. L. Adler, B. R. Stone, P. D. Zajac: Amplification of high-order rainbows of a cylinder with an elliptical cross section, Appl. Opt. **37**, 1527 (1998)

19.146 C. L. Adler, J. A. Lock, J. Mulholland, B. Keating, D. Ekelman: Experimental observation of total-internal-reflection rainbows, Appl. Opt. **42**, 406 (2003)

19.147 S. D. Gedzelman: Simulating glories and cloudbows in color, Appl. Opt. **42**, 429 (2003)

19.148 P. Laven: Simulations of rainbows, coronas, and glories by use of Mie theory, Appl. Opt. **42**, 436 (2003)

19.149 J. A. Lock, L. Yang: Mie theory of the corona, Appl. Opt. **30**, 3408 (1991)

19.150 L. Cowley, Ph. Laven, M. Vollmer: Rings around sun and moon: coronae and diffraction, Physics Education **40**(1), 51–59 (2005)

19.151 K. Sassen: Iridescence in an aircraft contrail, J. Opt. Soc. Am. **69**, 1080 (1979)

19.152 K. Sassen: Corona producing cirrus clouds properties derived from polarization LIDAR and photographic analysis, Appl. Opt. **30**, 3421 (1991)

19.153 K. Sassen, G. G. Mace, J. Hallett, M. R. Poellot: Corona-producing ice clouds: A case study of a cold mid-latitude cirrus layer, Appl. Opt. **37**, 1477 (1998)

19.154 E. Tränkle, B. Mielke: Simulation of pollen coronas, Appl. Opt. **33**, 4552 (1994)

19.155 P. Parviaainen, C. F. Bohren, V. Mäkelä: Vertical elliptical coronas caused by pollen, Appl. Opt. **33**, 4548 (1994)

19.156 W. B. Schneider, M. Vollmer: Experimental simulationsof pollen coronas, App. Opt. **44**, 5746 (2005)

19.157 J. A. Shaw, P. J. Neiman: Coronas and iridescence in mountain wave clouds, Appl. Opt. **42**, 476 (2003)

19.158 S. D. Gedzelman, J. A. Lock: Simulating coronas in color, Appl. Opt. **42**, 497 (2003)

19.159 K. Sassen: Cirrus cloud iridescence: A rare case study, Appl. Opt. **42**, 486 (2003)

19.160 P. J. Neiman, J. A. Shaw: Coronas and iridescence in mountain wave clouds over northeastern Colorado, Bull. Am. Met. Soc. **84**(10), 1373–1386 (2003)

19.161 H. C. van de Hulst: A theory of the anti-coronae, J. Opt. Soc. Am. **37**, 16 (1947)

19.162 H. C. Bryant, A. J. Cox: Mie theory and the glory, J. Opt. Soc. Am. **56**, 1529 (1966)

19.163 M. J. Saunders: Near-field backscattering measurements from a microscopic water droplet, J. Opt. Soc. Am. **60**, 1359 (1970)

19.164 K. Sassen, W. P. Arnott, J. M. Barnett, S. Aulenbach: Can cirrus clouds produce glories?, Appl. Opt. **37**, 1427 (1998)

19.165 M. Vollmer: Effects of absorbing particles on coronas and glories, App. Opt. **44**, 5658 (2005)

19.166 Ph. Laven: Atmospheric glories: Simulations and observations, Appl. Opt. **44**, 5667 (2005)

19.167 W. Tape: *Review on Halos*, as introduction in [19.64]

19.168 A. B. Fraser: What size of ice crystals causes the halos?, J. Opt. Soc. Am. **69**, 1112 (1979)

19.169 C. Knight, N. Knight: Snow crystals, Sci. Am. **228**, 100 (1973)

19.170 W. A. Bentley, W. J. Humphreys: *Snow Crystals* (Dover, New York 1962) reprint of 1931

19.171 R. Sussmann: Optical properties of contrail-induced cirrus: Discussion of unusual halo phenomena, Appl. Opt. **36**, 4195 (1997)

19.172 C. S. Hastings: A general theory of halos, Monthly Weather Rev. **48**, 322 (1920)

19.173 W. Tape, G. P. Können: A general setting for halo theory, Appl. Opt. **38**, 1552 (1999)

19.174 F. Pattloch, E. Tränkle: Monte Carlo simulation and analysis of halo phenomena, J. Opt. Soc. Am. A **1**, 520 (1984)

19.175 E. Tränkle, R. G. Greenler: Multiple-scattering effects in halo phenomena, J. Opt. Soc. Am. A **4**, 591 (1987)

19.176 M. Pekkola: Finnish halo observing network: Search for rare halo phenomena, Appl. Opt. **30**, 3542 (1991)

19.177 R. Greenler: Sunlight, ice crystals, and the sky archaeology, Proc. Roy. Inst. Great Britain **65**, 47 (1994)

19.178 G. P. Können: Polarization and intensity distributions of refraction halos, J. Opt. Soc. Am. **73**, 1629 (1983)

19.179 G. P. Können, J. Tinbergen: Polarimetry of a 22° halo, Appl. Opt. **30**, 3382 (1991)

19.180 G. P. Können, A. A. Schoenmaker, J. Tinbergen: A polarimetric search for ice crystals in the upper atmosphere of venus, Icarus **102**, 62 (1993)

19.181 G. P. Können: Symmetry in halo displays and symmetry in halo-making crystals, Appl. Opt. **42**, 318 (2003)

19.182 G. P. Können, H. R. A. Wessels, J. Tinbergen: Halo polarization profiles and sampled ice crystals: Observations and interpretation, Appl. Opt. **42**, 309 (2003)

19.183 E. Boeker, R. van Grondelle: *Environmental Science* (Wiley, New York 2001)

19.184 R. Wilson: The blue sun of 1950 September, Mon. Not. R. Astron. Soc. **111**, 478 (1951)

19.185 E. O. Hulburt: Explanation of the brightness and color of the sky, particularly the twilight sky, J. Opt. Soc. Am. **43**, 113 (1953)

19.186 M. Vollmer: Estimating the Thickness of the Atmosphere by Rayleigh Scattering, Am. J. Phys. **71**, 979–983 (2003)

19.187 F. E. Volz: Zenith polarization and color ratio during twilight, Appl. Opt. **20**, 4172 (1981)

19.188 K. L. Coulson: Effects of the El Chichon volcanic cloud in the stratosphere on the polarization of light from the sky, Appl. Opt. **22**, 1036 (1983)

19.189 F. G. Fernald, B. M. Herman, J. A. Reagan: Determination of aerosol height distributions by lidar, J. Appl. Meteor. **11**, 482 (1972)

19.190 F. G. Fernald: Analysis of atmospheric LIDAR observations: Some comments, Appl. Opt. **23**, 652 (1984)

19.191 J. D. Klett: Lidar inversion with variable backscatter/extinction ratios, Appl. Opt. **24**, 1638 (1985)

19.192 J. Bosenberg, D. Brassington, P. C. Simon (Eds.): *Instrument Development for Atmospheric Research and Monitoring: Lidar Profiling, DOAS and Tunable Diode Laser Spectroscopy* (Springer, Berlin, Heidelberg 1997)

19.193 Y. Liu, K. Voss: Polarized radiance distribution measurements of skylight II: Experiment and data, App. Opt. **36**, 8753 (1997)

19.194 R. L. Lee: Twilight and daytime colors of the clear sky, Appl. Opt. **33**, 4629 (1994)

19.195 R. L. Lee: Horizon brightness revisited: Measurements and a model of clear sky radiances, Appl. Opt. **33**, 4620 (1994)

19.196 J. R. Linskens, C. F. Bohren: Appearance of the sun and moon seen through clouds, Appl. Opt. **33**, 4733 (1994)

19.197 R. L. Lee: Digital imaging of clear sky polarization, Appl. Opt. **37**, 1465 (1998)

19.198 R. L. Lee, J. Hernández-Andrés: Measuring and modeling twilight's purple light, Appl. Opt. **42**, 445 (2003)

19.199 J. Hernández-Andrés, R. L. Lee, J. Romero: Color and luminance asymmetries in the clear sky, Appl. Opt. **42**, 458 (2003)

19.200 R. L. Lee, J. Hernández-Andrés: Colors of the daytime overcast sky, Appl. Opt. **44**, 5712 (2005)

19.201 N. Thomas, W. J. Markiewicz, R. M. Sablotny, M. W. Wuttke, H. U. Keller, J. R. Johnson, R. J. Reid, P. H. Smith: The color of the martian sky and its influence on the illumination of the martian surface, J. Geophys. Res. **104**, 48795 (1999)

19.202 http://cfa-www.harvard.edu/hitran/l, http://www.hitran.com

19.203 C. S. D. Ahrens: *Meteorology Today*, Vol. 4 (West Publ. Comp., St. Paul 1991)

19.204 C. F. Bohren: Multiple scattering of light and some of its observable consequences, Am. J. Phys. **55**, 524 (1987)

19.205 H. Koschmieder: Theorie der horizontalen Sichtweite, Beitr. Phys. freien Atmosphäre **XII**, 33 (1924) in German

19.206 H. Koschmieder: Theorie der horizontalen Sichtweite II: Kontrast und Sichtweite, Beitr. Phys. freien Atmosphäre **XII**, 171 (1925) in German

19.207 S. Q. Duntley: The reduction of apparent contrast by the atmosphere, J. Opt. Soc. Am. **38**, 179 (1948)

19.208 N. Mason, P. Hughes: *Introduction to Environmental Physics* (Taylor and Francis, London 2001)

19.209 M. Z. Jacobson: *Atmospheric Pollution* (Cambridge Univ. Press., Cambridge 2002)

19.210 G. E. Shaw: Observations and theoretical reconstruction of the green flash, Pure Appl. Geophys. **102**, 223 (1973)

19.211 A. T. Young: Green flashes and mirages, Opt. Photon. News **10**, 31 (1999)

19.212 F. H. Ludlam: Noctilucent clouds, Tellus **IX**, 341 (1957)

19.213 M. Gadsden, W. Schröder: *Noctilucent Clouds* (Springer, Berlin, Heidelberg 1989)

19.214 G. E. Thomas: Noctilucent clouds, Rev. Geophys. **29**, 553 (1991)

19.215 M. Littmann, K. Willcox: *Totality, Eclipses of the Sun* (Univ. Hawaii Press, Honolulu 1991)

19.216 P. S. Harrington: *Eclipse* (Wiley, New York 1997)

19.217 G. E. Shaw: Sky brightness and polarization during the 1973 African eclipse, Appl. Opt. **14**, 388 (1975)

19.218 G. P. Können: Skylight polarization during a total solar eclipse: A quantitative model, J. Opt. Soc. Am. A **4**, 601 (1987)

19.219 E. H. Geyer, M. Hoffmann, H. Volland: Influence of a solar eclipse on twilight, Appl. Opt. **33**, 4614 (1994)

19.220 K.-P. Möllmann, M. Vollmer: Measurements and predictions of the illuminance during a solar eclipse, Eur. J. Phys. **27**, 1299–1314 (2006)

19.221 D. K. Lynch: Optics of sun beams, J. Opt. Soc. Am. A **4**, 609 (1987)

19.222 W. Livingston, D. Lynch: Mountain shadow phenomena, Appl. Opt. **18**, 265 (1979)

19.223 D. K. Lynch: Mountain shadow phenomena 2: The spike seen by an off-summit observer, Appl. Opt. **19**, 1585 (1980)

19.224 H. E. Ross, C. Plug: *Thy Mystery of the Moon Illusion* (Oxford Univ. Press, Oxford 2002)

19.225 G. R. Lockhead, Myron L. Wolbarsht: Toying with the moon illusion, Appl. Opt. **30**, 3504 (1991)

19.226 S.-I. Akasofu: The dynamic aurora, Sci. Am. **261**, 54 (May 1989)

19.227 J. A. Whalen, R. R. O'Neil, R. H. Pritchard: The aurora. In: *Handbook of Geophysics and the space environment*, ed. by A. S. Jursa (Air Force Geophysics Laboratory, US Air Force 2001) Chap. 12

19.228 R. Feynman: *The Feynman Lectures on Physics*, Vol. II (Addison Wesley, San Francisco 1963) Chap. 9

19.229 M. A. Uman: *Lightning* (Dover, New York 1984) reprint of 1969 ed. by Mc Graw Hill

19.230 E. R. Williams: The electrification of thunderstorms, Sci. Am. **260**, 48 (Nov. 1988)

19.231 W. A. Lyons, R. A. Armstrong, E. A. Bering III, E. R. Williams: The hundred year hunt for the sprite, EOS Trans. Am. Geophys. Union **81**, 373 (2000)

19.232 M. Rodriguez: Triggering and guiding megavolt discharges by use of laser-induced ionized filaments, Opt. Lett. **27**, 772–774 (2002)

19.233 P. Moore: *The Data Book of Astronomy* (IOP, Bristol 2000)

19.234 J. B. Kaler: *Astronomy* (Harper Collins, New York 1994)